UNIVERSITÀ DEGLI STUDI
DI MODENA E REGGIO EMILIA

Dottorato di ricerca in Neuroscienze

in convenzione con l'Università degli Studi di Parma

Ciclo XXXIV

"Two- and Three-terminal Organic Neuromorphic devices: benchside demonstration, analytical models and ion sensing applications"

Candidato: Gioacchino Calandra Sebastianella

Relatore (Tutor): Prof. Fabio Biscarini

Correlatore (Co-Tutor): Prof. Michele Zoli

Coordinatore del Corso di Dottorato: Prof. Michele Zoli

"...alla mia famiglia"

Abstract

Organic electronics is the eligible technology towards the development of devices able to be interfaced with the living matter, paving the way for *in vivo* real-time signal processing and selective quantification of neurotransmitters in pathological condition like Parkinson's disease. Organic electronic devices cover a wide range of applications due to their features such as low energy consumption, high tunability, biocompatibility, flexibility and the capability to mix electronic and ionic conductivity, making them especially suited for operations in electrolyte solutions, providing new opportunities for medical diagnostics and therapy. This entanglement between ionic transport (a slow process), and electronic currents (fast processes), is at the origin of one of the most promising feature of organic electronic devices: Neuromorphism.

Organic neuromorphic electronics aims at developing hybrid brain-inspired computing/memory units able to process and store information in the same space, thus overcoming the spatial limitations of silicon-based circuits based on von Neumann architectures.

The aim of this thesis is to investigate the fundamental and translational aspects of the neuromorphic response in organic electronic devices.

In particular, Short-Term Plasticity (STP) is investigated in three-terminal architectures (i.e. Electrolyte-Gated Organic Transistors – EGOTs) and in artificial synapses built on intracortical microelectrodes.

This work demonstrates, on the one hand, that STP can be elicited between the two contacts of the semi-conductive channel of an EGOT, while a third electrode enables the modulation of amplitude and characteristic time scale of the neuromorphic response. This approach allows the operator to arbitrarily set the baseline and the steady-state current,

preluding to multilevel memory writing and coexistence of both depressive and facilitative response in frequency-driven EGOTs.

On the other hand, this work shows the existence of a frequency-dependent crossover between facilitative and depressive regimes in implantable artificial synapses. STP features are described with an RLC equivalent circuit unveiling the physical origin and enabling the prediction of the artificial synapse response.

Finally, neuromorphic devices are demonstrated as specific label-free ion and neurotransmitters sensors, rationalizing their multi-parametric response by means of the theoretical and analytical platform developed in this thesis.

L'elettronica organica è la tecnologia idonea per lo sviluppo di dispositivi in grado di interfacciarsi con la materia vivente, aprendo la strada all'elaborazione del segnale *in vivo* in tempo reale e alla quantificazione selettiva dei neurotrasmettitori in condizioni patologiche come il morbo di Parkinson. I dispositivi elettronici organici coprono un'ampia gamma di applicazioni grazie alle loro caratteristiche come basso consumo energetico, vasta gamma di variabilità, biocompatibilità, flessibilità e capacità di combinare conduttività elettronica e ionica, rendendoli particolarmente adatti per operazioni in soluzioni elettrolitiche, fornendo nuove opportunità per la diagnosi e terapia medica. Questo intreccio tra trasporto ionico (processo lento) e correnti elettroniche (processi veloci), è all'origine di una delle caratteristiche più promettenti dei dispositivi elettronici organici: il neuromorfismo.

L'elettronica organica neuromorfica mira a sviluppare unità di calcolo/memoria ibride ispirate al cervello in grado di elaborare e memorizzare informazioni nello stesso spazio, superando così le limitazioni spaziali dei circuiti a base di silicio basati su architetture di von Neumann.

Lo scopo di questa tesi è indagare gli aspetti fondamentali e traslazionali della risposta neuromorfica in dispositivi elettronici organici.

In particolare, la Plasticità a Breve Termine (STP) viene studiata in architetture a tre terminali (es. Electrolyte-Gated Organic Transistor – EGOT) e in sinapsi artificiali costruite con microelettrodi intracorticali.

Questo lavoro dimostra, da un lato, che la STP può essere indotta tra i due contatti del canale semiconduttivo di un EGOT, mentre un terzo elettrodo consente la modulazione dell'ampiezza e della scala temporale caratteristica della risposta neuromorfica. Questo approccio consente all'operatore di impostare arbitrariamente la linea di base e la corrente

allo stato stazionario, preludendo alla scrittura multilivello della memoria e alla coesistenza di risposte sia depressive che facilitative negli EGOT controllati in frequenza. D'altra parte, questo lavoro evidenzia l'esistenza di una transizione frequenza-dipendente tra regime facilitativo e depressivo in sinapsi artificiali impiantabili. Le caratteristiche STP sono state descritte con un circuito equivalente RLC svelandone l'origine fisica e abilitando la predizione della risposta sinapsi artificiale.

Infine, i dispositivi neuromorfici sono dimostrati come specifici sensori di ioni e neurotrasmettitori in assenza di elementi di riconoscimento, razionalizzando la rispettiva risposta multiparametrica mediante la piattaforma teorica e analitica sviluppata in questa tesi.

Contents

1. Introduction

This introductive chapter presents Organic Bioelectronics as an emerging scientific, technological and disciplinary field, giving an overview on its development, technological applications and future perspectives. In particular, *Neuromorphic* response of Organic Bioelectronic devices is discussed as one of the most promising feature of the field, in relationship with the relevant features of the nervous system that can be mimicked by organic bioelectronic devices.

1.1 Organic Electronics

Organic electronics (O.E.) is a scientific field based on the study of organic (semi-)conductive materials and on their usage in technological applications. O.E. devices are particularly promising candidates for the substitution/integration of silicon-based devices thanks to their flexibility, stretchability and softness[1]. Nowadays, the most mature organic electronics technologies are:

- OLEDs (Organic light-emitting diodes) (figure 1.1a) which are already available for commercial use and represent cutting-edge display technology[2]. In OLEDs, the light-emitting layer is constituted by organic semi-conductors;
- OPVs (Organic photovoltaics or organic solar cells) (figure 1.1b) where, upon illumination, charge separation is induced in a photoactive layer (usually a blend of organic semi-conductors) resulting in the elicitation of a potential difference;
- OFETs (Organic Field-Effect Transistors), amplifiers in which the conductance of an organic semi-conductive layer can be arbitrarily tuned, that find their way into many applications likewise logic circuiting, mechanical sensing and imaging (figure 1.1 c-e)[3].

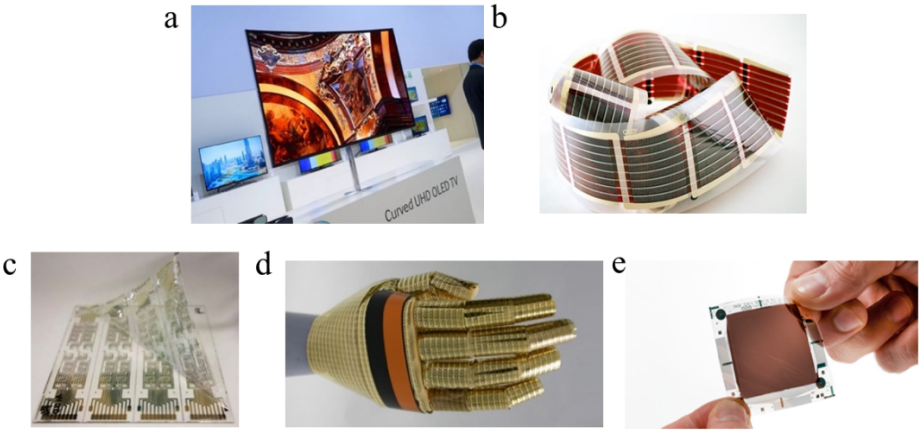

Figure 1.1 a) UHD OLED TV; b) Printed organic solar cells modules; c) Photograph of organic CMOS logic circuit on a one-micron (μm) substrate; d) OFET as mechanical sensor; e) OFET X-ray sensors for image sensing applications.

Such vastness of applicability allows to envision a future in which Organic Electronics will become predominant in the electronic market[4], due to its constant growth coupled with its capability to provide novel technological approaches in the field of electronics.
Furthermore, Organic Electronics is a multidisciplinary scientific field which poses important questions both from a fundamental and an applicative point of view, inherently demanding the collaborative effort of chemists, physicists, engineers and many other scientists towards the common goal of advancing knowledge.

1.2 Organic Biolectronics: introduction

One of the most fruitful examples of such collaborative efforts - enabled by the above described technological/scientific platform - is Organic bioelectronics, which stands at the convergence between O.E. and biology. It concerns the integration between organic electronic devices with biological systems, which ultimately results in the development of devices which are capable to operate in liquid/wet environment (i.e. electrolyte solutions), preferably showing mixed electronic/ionic conductivity.
Organic Bioelectronic devices are envisioned to be implanted, weared or attached to skin or tissue, providing advantageous opportunities for medical diagnostics and therapy[5]. Following such vision, a number of different device architectures has been developed (figure 1.2), including bioelectronic noses[6], electrophysiological sensors[7–16], electrocardiogram sensors[17], electronic skins[18–23], wireless pressure devices[24–26] and motion sensors[27].

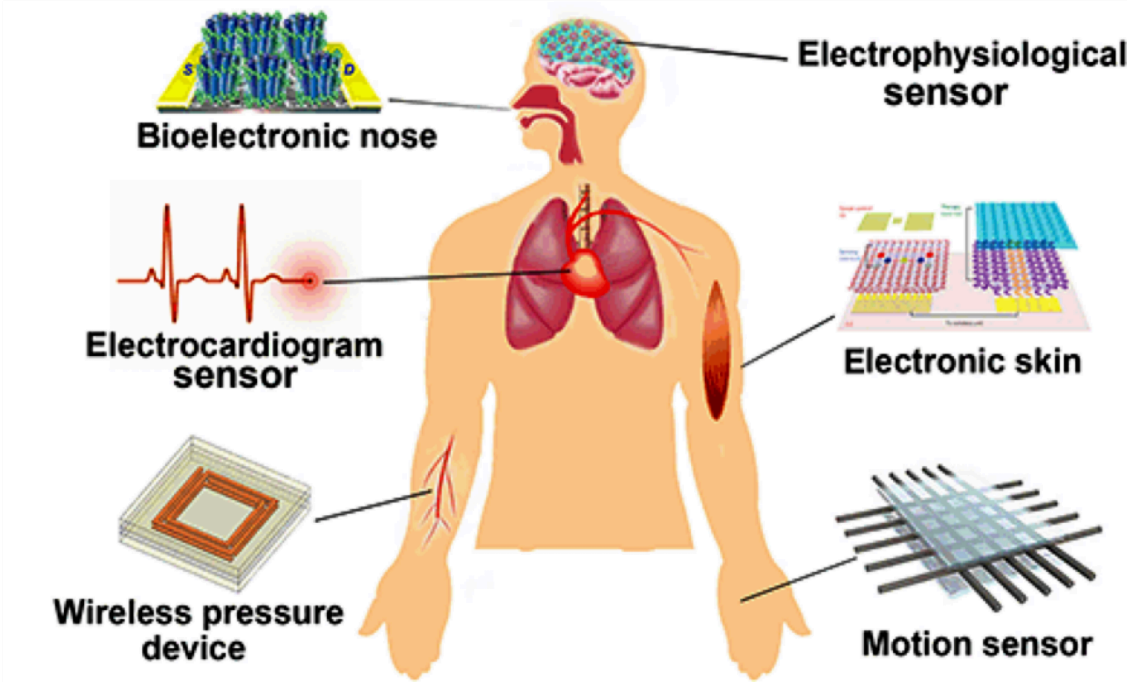

Figure 1.2 Overview of organic bioelectronic devices operating at the interface with the human body for diagnostic/monitoring purposes. In clockwise order from top left: bioelectronic nose, electrophysiological sensor, electronic skin, motion sensor, wireless pressure sensor and electrocardiogram sensor. (Figure from *Yang et al 2013, Nano Res.* ***10****, 1560–1583 (2017)*[5])

1.3 Organic Bioelectronics: materials and devices

1.3.1 Organic Mixed Ionic-Electronic Conductors

The ambition of interfacing electronic devices with the living matter poses strict constraints in terms of choice of active materials[28–30]. First of all, such materials should be biocompatible/non-toxic, capable of operating in flexible/conformable devices and stable in water for a sufficiently long amount of time in the absence of significant performance loss. Additionally, their resistance should be low enough to ensure functionality under driving voltages that fall within the electrochemical stability window of water, in order to avoid detrimental and harmful electrolysis reactions, and it also should be variable according to variations of electrolyte composition (e.g. for sensing and

transduction applications). Furthermore, they should ideally be processable with high-throughput and scalable technologies. These ambitious *desiderata* lead to the development of a novel class of materials, which can be collectively addressed as Organic Mixed Ionic-Electronic Conductors - OMIECs (figure 1.3)[31].

As suggested by the definition itself, OMIECs are materials that efficiently transport both ionic and electronic charges. They usually rely on a π-conjugated polymeric backbone, which ensures electronic conductivity, coupled with an ion-transporting phase. The nature of this coupling enables the classification of OMIECs in different categories, here briefly discussed and summarized.

Indeed, OMIECs can be classified according to two main distinctive features. The first one is the intrinsic content of ionic charge in the OMIEC structure, which allows to discriminate between OMIECs which own ionic charge (figure 1.3 (I,III,V)) and OMIECs which demand ionic charge injection (figure 1.3 (II,IV,VI); the second one is the homogeneity of the ionic and electronic transport, namely distinguishing between OMIECs in which transport occurs concurrently throughout the material if the material itself is homogeneous, and OMIECs which exhibit a physical separation between the ionic and electronic conductive regions, which can be either blended or block co-polymerized (figure 1.3 a,b), resulting in non-homogeneous transport.

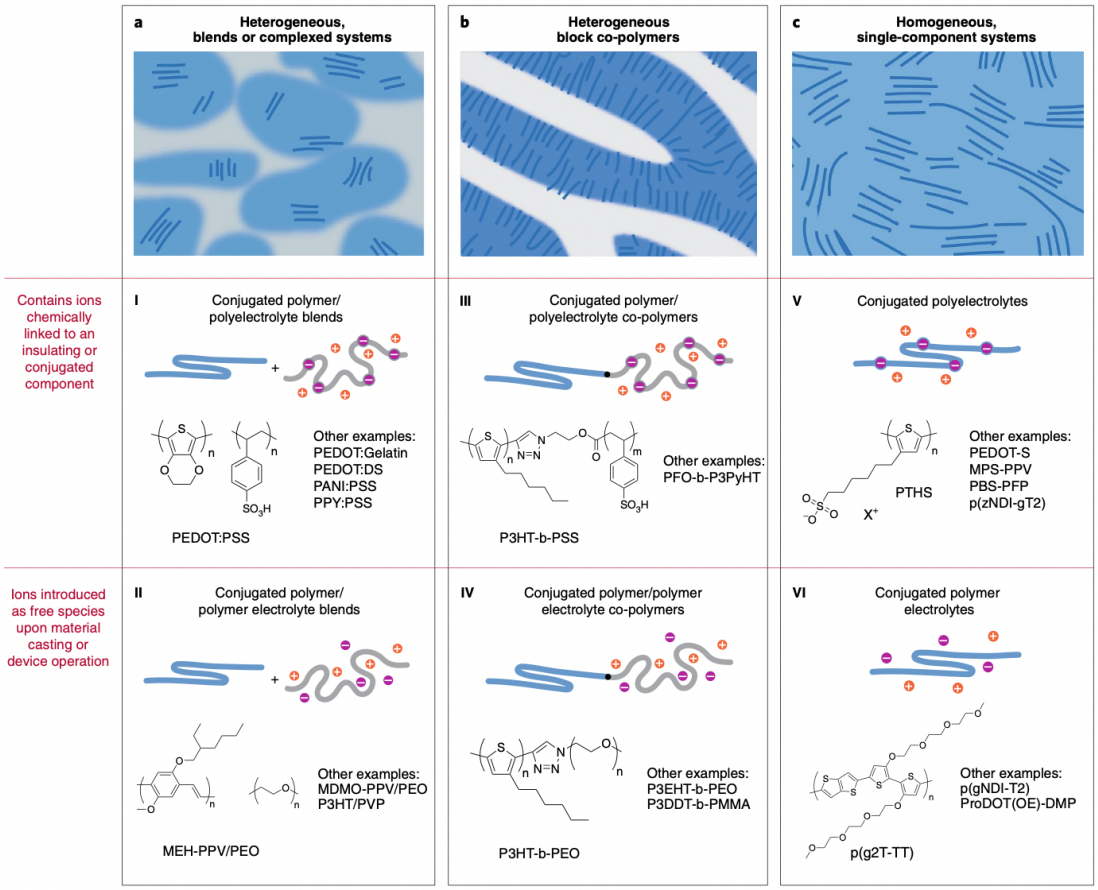

Figure 1.3 Different OMIECs categories. a) The figures (I and II) represent two cases of heterogeneous blends, largely disordered on multiple length scale, of an electronically conducting conjugated polymer with an ionic charge bearing polyelectrolyte and an ion solvating polymer electrolyte, respectively. b) heterogeneous block copolymers of an electronically conductive conjugated polymer with (III) an ionic charge-carrying polyelectrolyte or (IV) a solvating polymer electrolyte. Such block copolymers are often characterised by more well-defined pure phases and easily synthetized mesoscale ordering. c) fully conjugated ionic charge-bearing polyelectrolytes (V) and solvating polymer electrolytes (VI). (Figure from Paulsen et al. *Nat. Mater.* (2019)[31])

Besides being mandatory for certain technological applications (e.g. in batteries or capacitors), this entanglement between ionic and electronic currents is crucial also in bioelectronics, making OMIECs of central importance for the development of bioelectronic applications which demand an interplay between ionic and electronic charge, such as EGOTs (Electrolyte – Gated – Organic – Transistors) for the amplification of electrophysiological signals[32], ion pumps for the local release of specific drugs[33], and the most promising application of organic bioelectronics devices: neuromorphism[34].

Among OMIECs, a great interest is addressed to Poly(3,4-ethylenedioxythiophene):poly(styrene-sulfonate) (PEDOT:PSS) (figure 1.3.I and figure 1.4), whose stoichiometric form (PEDOT/PSS) is obtained via electrochemical polymerization of 3,4- ethylenedioxythiophene(EDOT). This oxidation process results in the presence of one positive charge *per* three EDOT units in the PEDOT backbone. To ensure electro-neutrality and water solubility the process is carried on in the presence of an excess of sodium poly(styrene-sulfonate)(Na+PSS-), whose PSS poly-anion compensates (upon a simple ionic exchange reaction) the charge of the PEDOT poly-cation, obtaining a neutral conductive material.

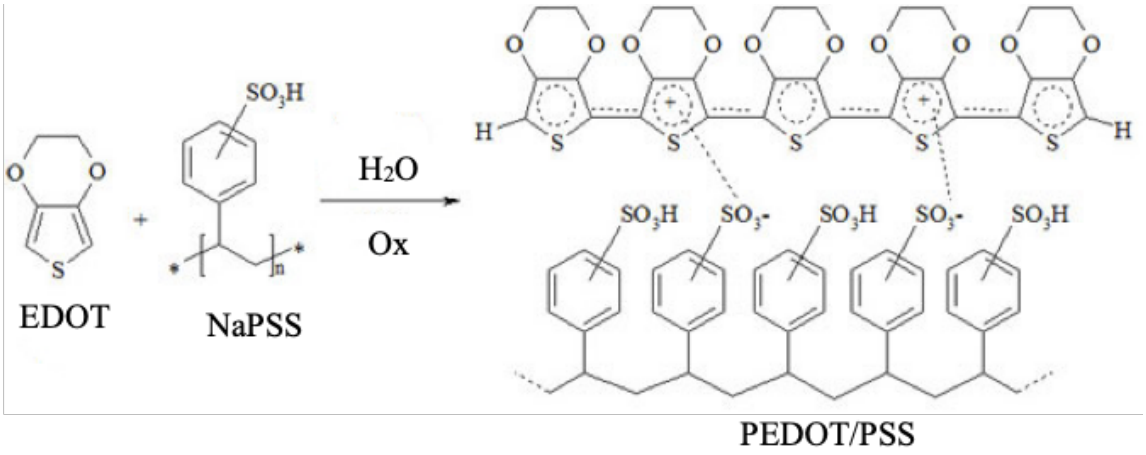

Figure 1.4 Synthesis and chemical structure of PEDOT/PSS.

Conductivity of PEDOT/PSS can be enhanced in several ways. All of them involve the use of additives, typically polar and high-boiling solvent (such as DMSO) and other moieties such as reticulating agents (e.g. glycidyloxypropyltrimethoxysilane - GOPS). There is a morphological reason underlying this conductivity enhancement: the additives allow the PEDOT to form large interconnected domains, thus reducing grain boundaries and facilitating hole transport.

1.3.2 Organic semiconductors

In the framework of technological applications of organic bioelectronics, besides OMIECs, organic semiconductors (OSCs) are largely employed as active layer materials. The features that make them attractive are: solution-processability, flexibility and lightweight[35].

OSCs are divided in two major groups of molecules: low molecular weight moieties and conductive polymers. Both categories feature extensively delocalized charge in π-conjugated systems. The π-orbital overlapping between two or more conjugated system facilitates electronic delocalization throughout the whole polymeric/molecular structure, lending in high charge carrier mobility. In their pristine state, OSCs are insulators and the operations necessary to increase their conductivity are:

- OSC oxidation/reduction;
- Field-effect doping by capacitive coupling with an external electrode through a dielectric thin-film or an electrolyte.

In function of the different kind of doping process the charge carriers can be:

- *Holes (h^+)* if the doping process results in the extraction of electrons from the OSC layer. These are termed *p-type* OSCs;
- *Electrons (e^-)* if the doping process results in the addiction of electrons to the OSC layer. These are termed *n-type* OSCs..

Among the most common organic semiconductors employed in organic bioelectronics, poly-acenes have been extensively studied. In particular, pentacene (figure 1.5a) and its derivatives are widely used in sensing application. Pentacene is a linear acene constituted by five condensed benzene rings; its semi-conductive properties arise from the extended conjugation of its π-orbitals. A soluble derivative of pentacene, used in this work of thesis,

is 6,13- bis(triisopropylsilylethynyl)pentacene (TIPS-P5) (figure 1.5b), in which the addiction of –C≡C–SiR_3 groups results in increased solubility in organic solvents, increased stability since they block oxidative degradation and facilitation of the interdigitated π-stacking between adjacent molecules in a polycrystalline structure, yielding an anisotropic charge transport[36]

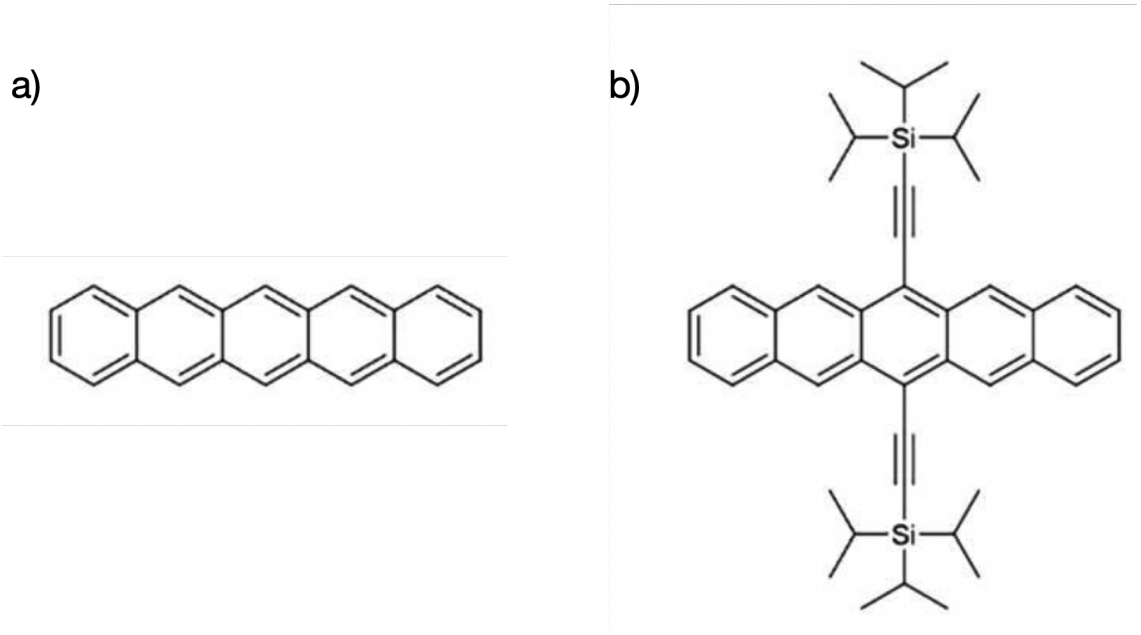

Figure 1.5 a) Pentacene and b) TIPS-P5 structure.

1.3.3 Electrolyte-Gated-Organic-Transistrors

The term Electrolyte-Gated-Organic-Transistors (EGOTs) is used to collectively refer to a family of three-terminals devices which share a common layout.

In particular, the EGOT architecture consists three electrodes, namely Source (S), Drain (D) and Gate (G), a channel made of an organic (semi)conductive material bridging the source and the drain, and an electrolyte solution ensuring the coupling between the channel and a third the gate. The potential applied to the gate electrode, placed in contact

with the electrolyte, leads to the modulation of the semiconductor conductivity. The application of a potential difference between the source and drain electrodes generates a current within the channel, which is a function of the channel conductivity and, hence, of the gate voltage.

Depending on the different material which constitutes the channel between Source and Drain electrodes is possible to differ: "depletion mode EGOT" and "accumulation mode EGOT", also called OECTs and EGOFETs, respectively. Typically, the OECT channel consists of an OMIEC, usually PEDOT:PSS, while the EGOFET exploits organic semiconductors (usually Pentacene and TIPS-Pentacene[37]). OECTs and EGOFETs schematic layouts are depicted in figure 1.6a and 1.6b.

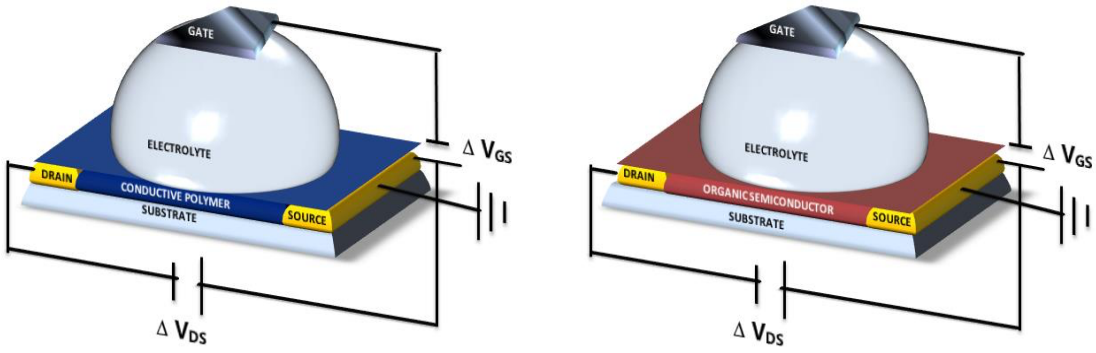

Figure 1.6 a-b) Schematic representation and connection layout of depletion EGOT (a) and accumulation EGOT (b), operated in common source-common ground configuration

The working principle of EGOTs is, with slight modifications, analogous to that of solid-state Organic Field Effect Transistors[38] (OFETs). In OFETs, the channel is coupled to the gate by means of a thin-layer of dielectric material, with the gate and the dielectric placed either below the semi-conductive channel (bottom gate) or on top of it (top gate). In *p*-

type OFETs the gate is negatively polarized ($V_{GS} < 0$), leading to accumulation of holes at the channel/dielectric interface. This process arises from the principle of electroneutrality, in order to compensate the negative charge that accumulates at the gate/dielectric interface consequently to the negative bias (figure 1.7 a)

Once the charges are accumulated in the semiconductive channel, the application of potential between source and drain electrodes ($V_{DS} < 0$) causes the flux of carriers from the source to the drain electrodes, where the current is measured. In *n-type* OFETs, conversely, the negative charge is accumulated at the semiconductor/dielectric interface upon the positive polarization of gate ($V_{GS} > 0$).

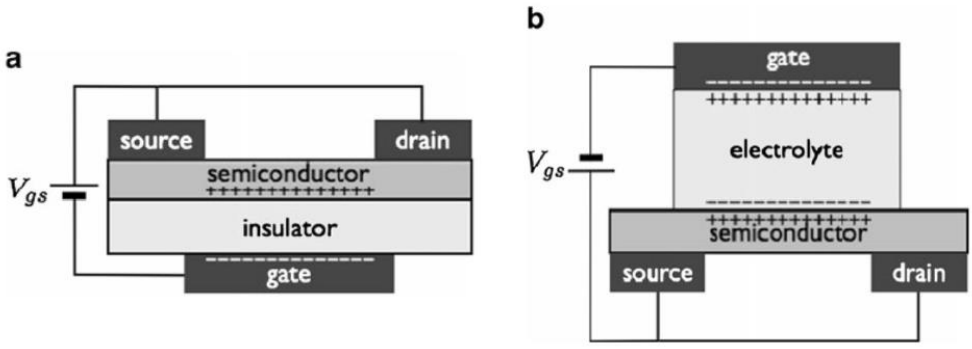

Figure 1.7 Representations of FET in bottom gate configuration (a) and top gate configuration of an EGOFET (b). (Figure from D. Wang et al., 2016[39])

In (organic) field effect transistors there are two operation regimes: the linear regime, in which the current and the voltage follow the Ohm law, and the saturation regime in which the current that flows is limited to a constant value which is a sole function of the gate voltage (while is independent of the drain voltage). The two regimes are described by the following equations:

Linear regime:

$$I_{DS} = \frac{W}{L} C_i \mu (V_{GS} - V_{th}) V_{DS} \qquad for\ V_{DS} < V_{GS} - V_{th}$$

Saturation regime:

$$I_{DS} = \frac{W}{2L} C_i \mu (V_{GS} - V_{th})^2 \qquad for\ V_{DS} \geq V_{GS} - V_{th}$$

The term W is the channel width and L the channel length [cm], C_i [F/cm^2] is the capacitance per unit area of the dielectric (i.e. solid or electrolyte), V_{th} is the threshold voltage [V], described as the gate voltage at which the field-effect takes place and the conductive channel in the semiconductor film is created, and μ is the field-effect mobility [cm^2/Vs] of the charge carriers.

In EGOTs, the dielectric is constituted by a small amount of electrolytic solution whose potential is set by the gate. As an example, in EGOT *p-type* devices, the application of a negative polarization at the gate electrode ($V_{GS} < 0$ V) causes the accumulation of cations at the gate/electrolyte interface (figure 1.7 b) and of anions at the semiconductor/electrolyte interface, resulting in the formation of electrical double layer (EDL) at both interfaces (figure 1.8).

Since the capacitance of the electrical double layers responsible of gating in EGOTs is orders of magnitude higher than the one of silicon oxide commonly used as gate dielectric in OFETs, EGOTs can be operated with ultra-low voltages ($|V_{GS}| < 1$V) and are capable of amplifying small potential differences into high currents.

The main advantages of EGOTs, which make them suitable for label free sensing and electrophysiological transduction, are the high potentiometric sensitivity and the possibility to integrate highly selective biological moieties on the gate electrode, resulting in high selectivity of the device response. EGOTs are nowadays widely studied as electronic biosensors able to detect a very large ensemble of biomolecular targets involved in the diagnostics of diseases, ranging from proteins or nucleotide sequences to small organic molecules in bodily fluids[40].

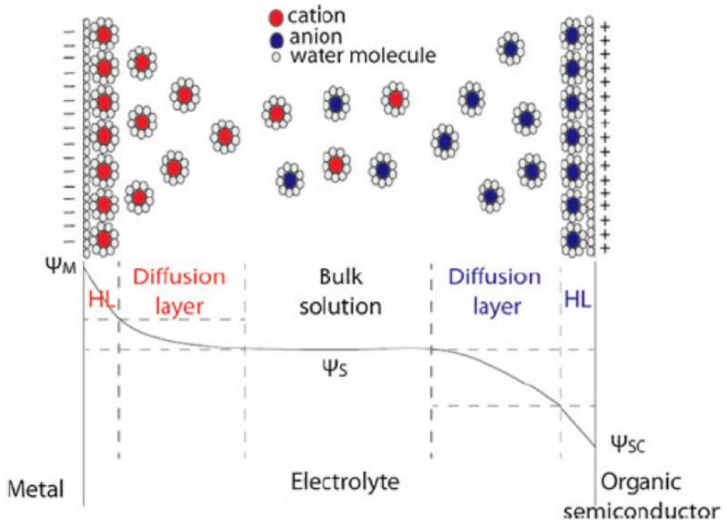

Figure 1.8 Schematic representation of EDL formation in an EGOFET, with Helmholtz layer (HL), diffuse layer and associated potential profile (black line) (D. Wang et al., 2016[39]).

1.4 Neural processing: an overview

Contemporary society is largely based on the grounds of information technology, and we rely on computing architectures, virtually, for any aspect of our lives, in a constantly growing trend of integration between humanity and computers. Fostering this integration demands an effort in the direction of making computers similar to humanity, in particular in the way of "thinking", and this effort results in the field of Neuromorphic electronics. Being prone to direct integration with the living matter, organic bioelectronic devices are ideal candidate building blocks in the development of such a technological platform. To understand which device functions should be exploited in to this end, it is of utmost importance to understand how the brain works, especially concerning "data processing". The human brain is the main organ constituting the nervous system (NS), together with the spinal cord. It is a gelatinous mass with a weight of about 1500 g[41] which performs complex functions, receiving and elaborating the external information collected by the sense organs. It is also the "human" computer, whose data processing is realized by an

intercorrelated network of about 10^{11} neurons and 10^{15} synapses, where the neurons are the processing units[42].

The first image of a neuron was obtained by Santiago Ramón y Cajal in 1906 via the Golgi silver impregnation technique (figure 1.9). The ramified structure suggests the capability of neurons to create a complex network where transmission, memorization and computation of information occur simultaneously.

Figure 1.9 The Golgi silver impregnation technique is a simple histological procedure that reveals complete three-dimensional neuron morphology. This method is based in the formation of opaque intracellular deposits of silver chromate obtained by the reaction between potassium dichromate and silver nitrate (black reaction). Figure from "The Golgi silver impregnation method: commemorating the centennial of the Nobel Prize in medicine (1906) shared by Camillo Golgi and Santiago Ramón y Cajal".

The cellular body of neurons is called soma. Starting from the soma arise different ramifications, which can be classified according to their length and diameter. The axon is the bigger one, both in terms of length and diameter, and it is mainly responsible for

the transmission of electrical signals to other neurons, while the smaller ramifications are called dendrites. Dendrites are responsible for connection with other neurons (synapsis) both for collecting and transmitting signals (figure 1.10).

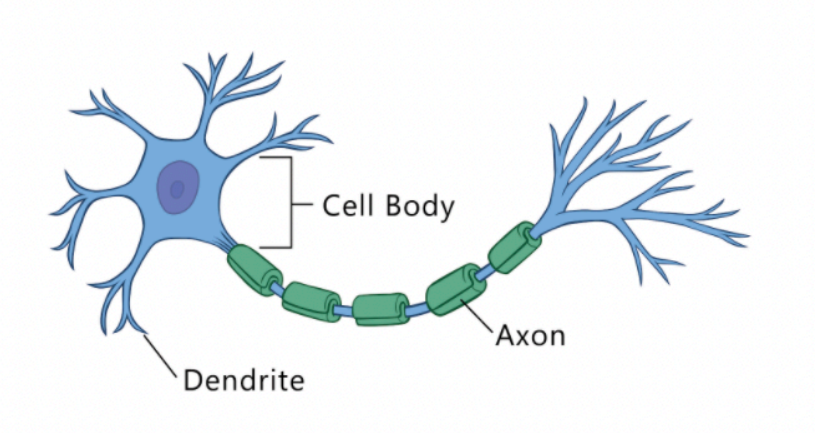

Figure 1.10 Neuronal cell structure [figure from http://www.thepartnershipineducation.com]

The communication between two neurons occurs through electrical pulses, also called *spikes,* in specific neuronal regions called synapsis where two neurons come into contact with each other. In the resting condition the neuron transmembrane potential value is at -70 mV; a spike event takes place when the resting potential overcomes a sub-threshold potential at -55 mV. Once the spike is triggered, the potential membrane increases to its max value around 30 mV (depolarization process); after reaching the max value, the potential membrane is then repolarized to -90 mV (refrectary period) and finally the potential returns to the resting value[43] (figure 1.11). Given the number of synaptic connections and the speed of the spiking process, the brain features massive parallel computing capabilities: the amount of information stored in a synapse is up to 4.7 bit, meaning that in 1 second 1 petabyte of data can be interchanged *via* the whole brain[44].

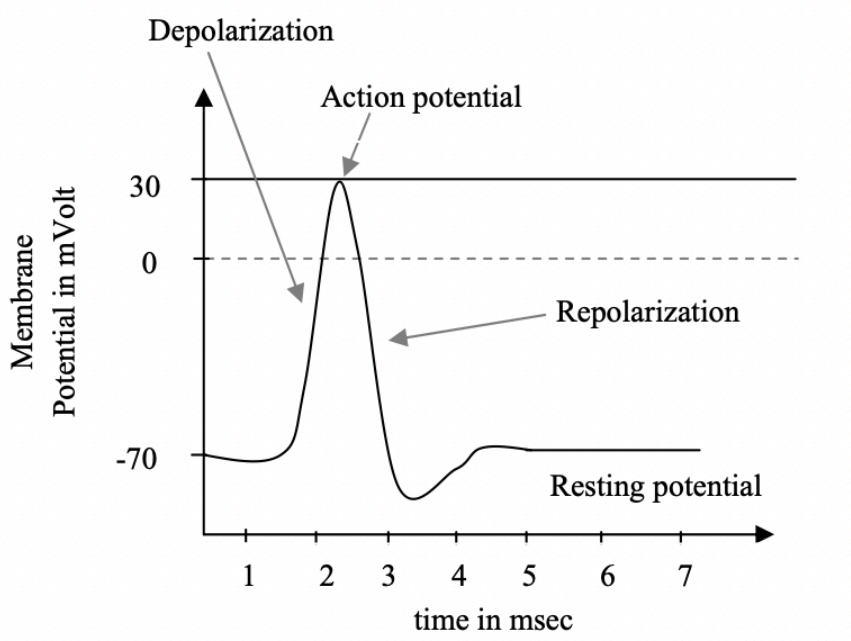

Figure 1.11 Single spike action potential and its phases: Depolarization, Repolarization and Resting Potential. Figure from "Kakoty et al. *IAES Int. J. Robot. Autom.* **2**, 1 (2012)[43].

If mimicked by artificial devices, this extremely good computational power, coupled with high energetic efficiency (~ 20 W), would be the key to create the new generation of technological system for data storage and transmission of information. A crucial enabling mechanism used by our brain to reach such outstanding performances, especially in learning and memorizing, is *synaptic plasticity*[45,46].

1.5 Synaptic plasticity

The synaptic plasticity consists in the ability of a synapse to increase or decrease its activity by means of repeated stimulation[47]. In a synaptic process the action potential is transmitted from the presynaptic to the postsynaptic neuron by means of neurotrasmitters. Such moieties, involving both small organic molecules and ionic species like Ca^{2+}, Na^{+} and K^{+}, have the role to carry the information, (figure 1.12). Every synapse possesses a

defined amount of neurotransmitters. Each spike activates a fraction of these resources, and the used fraction of neurotransmitter is then recovered with a characteristic time.

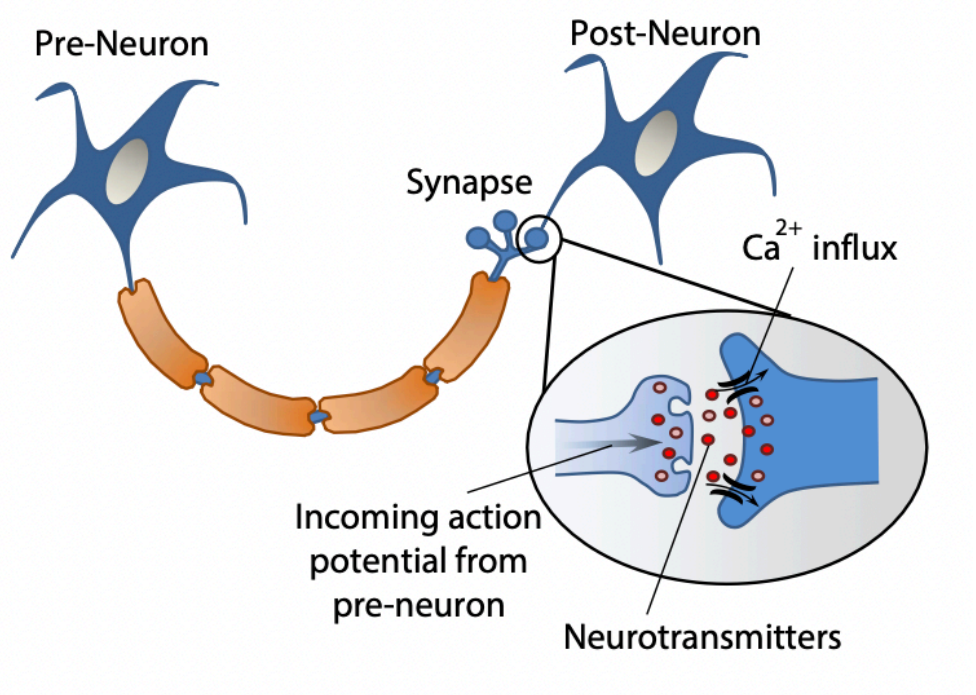

Figure 1.12 Biological process that depict the complessive synaptical event. Once fired the action potential induced the opening of the calcium channels allowing the releasing of the neurotrasmitters like dopamine, serotonin, noradrenaline etc. etc. Figure from Kelley et al. *Front. Hum. Neurosci.* **7**, 1–9 (2013)[46].

As a consequence, synaptic plasticity depends on the time scale on which the input is processed. It can be differentiated in short-term synaptic plasticity, which lasts on a time scale of tens of milliseconds to a few minutes, and long-term memory, from minutes, hours to years[46].

Short term plasticity (STP) can be further diversified, discriminating between the increase of its strength with time (facilitation and augmentation behavior), due to the elevation of calcium levels which increases the probability of vesicle fusion and the correspondent decrease (depressive behavior), consisting in an causing the overall depletion of vesicles for the release of neurotrasmitters[48–50]. The expression of specific types of filtering is

thought to depend on whether components of short-term enhancement or short-term depression dominate synaptic dynamics[51,52].

Once the information is "filtered" by this synaptic filter, it is temporally stored in the "working memory" involved in the selection, initiation and termination of information processing tasks[53].

Working memory integrates information from various subsequent synaptic-filtered stimuli, and performs the selection of a course of action among several alternatives: the "decision making"[54].

The last step of information processing concerns the "long term memory", which consists in the storage of information for an indefinite time, which affects our future behavior and upcoming choices (figure 1.13).

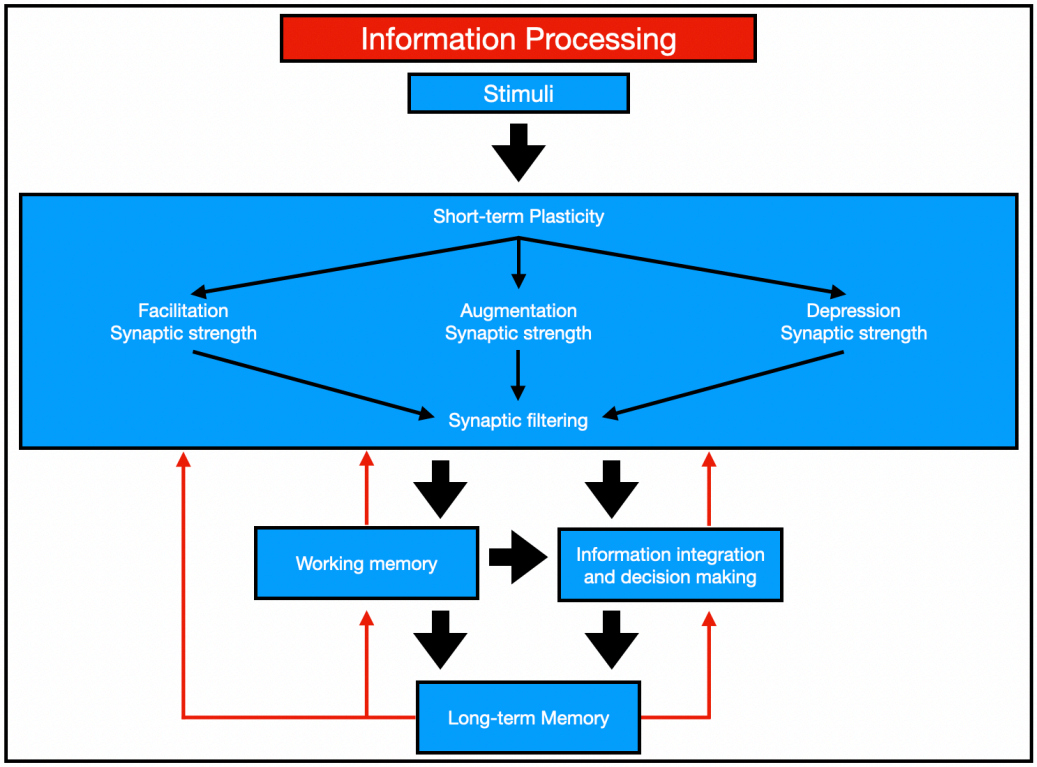

Figure 1.13 Model of STP functions in synaptic computations and information processing. Wide black arrows and narrow black arrows indicate information flow directions; red arrows show the factors that may influence information processing. Adapted figure from Deng et al. *Commun. Integr. Biol.* **4**, 543–548 (2011)[55].

1.6 Brain functions mimicking

In order to reproduce and mimic the brain functions, it is of primary importance to mimic the way in which neurons, its single units, work and communicate between each other *via* synapses.

The first mathematical analytical model of the neural network behavior was described in 1943 by Warren McCulloch and Walter Pitts[56], who introduced the "all-or-none" nature of nervous activity, where neural events and the relation among them can be treated by means of propositional logic.

In 1952 Hodgkin and Huxley proposed a complex description of the action potential propagation by studying the giant squid axons, describing both the transient nature of the neuronal impulse (spike) and the chemical details related to the fluxes of sodium and potassium ions involved in spike generation and propagation[57]. A significant advance in the mimicking of brain functions occurred through the introduction of artificial neural network (ANNs). The first example of ANN is a binary classifier, the “perceptron”[58]. Artificial neural networks (ANNs) aim at processing and storing information by mimicking the operation mode of actual neuronal networks. In particular, recognition patterns are stored in the synaptic weights (i.e. synaptic strength). The variation of synaptic weights is at the base of the learning process of ANNs. The basic learning process of ANNs consists in the training and systematic modification of the synapses in order to gradually obtain the resultant outputs. One important limitation of the single-layered perceptron ANN is the inability to perform non-linear logic operations (XOR for example). This shortcoming was overcome by the introduction of a multilayer perceptron (MLP). The MLP is the first case of a deep network able to model non-linear functions (e.g. XOR) in opposition to a single layer[59]. Each layer is made up of neurons; the neurons of two consecutive layers are connected by weighted synapses[60]. These weights are

usually randomly initialized and updated iteratively according to a suitable learning algorithm. In such systems, the last layer is *de facto* a function of all the previous layers. One major problem with MLP, and multilayered ANNs in general, is the large computational cost due the employing of a huge number of "synapses" and the need for large datasets required for the learning process. The availability of large datasets and computational resources allows to employ ANNs to solve many practical problems.

1.7 (Organic) Neuromorphic electronics

Despite the success of ANNs in applications, they are still far from mimicking the actual brain functions. The primary goal of neuromorphic electronics is to create autonomous machines that can interpret the world around them and make immediate decisions with high energy efficiency; to this end, it may be more efficient to develop algorithms and computing architectures that are directly inspired by the human brain neurobiological "hardware" structure. On an hardware level, the vast majority of computational infrastructures work according to the well-known Von Neumann architecture, which exhibits performance limitations in terms of speed and energy consumption, due to the separation of CPU and memory: this physical separation is often referred to as the "von Neumann bottleneck[61]". In order to overcome this inherent limitation, a novel class of computing devices has been envisioned, aimed at mimicking the computational power and the efficiency of human brain, in which computation and memory occur in the same physical space and with the same building blocks, namely a system of artificial neurons interconnected via artificial synapses. Due to this operational parallelism, such devices have been termed "Neuromorphic systems" by their pioneer, Carver Mead who in 1990 created the first neuromorphic circuit, consisting of polarized transistors operating in the subthreshold region[62,63].

Within this context, OMIECs have been proposed as active materials for neuromorphic applications, giving rise to the field of organic neuromorphic electronics[64,65].

Since ion drift is typically slower than electronic transport, there is a kinetic unbalance between the two main transport process occurring in OMIECs. As a consequence, OMIEC-based devices are out-of-equilibrium systems whose response depends on the device history or on frequency features of the input signals. Harnessing the dynamic interplay of ions/electrons, OMIEC-based devices can be engineered in neuromorphic electronic systems[66], developing computational architectures aimed at matching the energetic efficiency of the brain[67]. Neuromorphic organic devices can emulate brain functions at the single device unit level[68,69] and exhibit the most relevant features of synaptic data processing: short-term plasticity – STP[70,71], long- term potentiation – LTP[65,72–74] – and spike-timing dependent plasticity – STDP[75–81], with good electrical stability[82] and endurance[83].

Furthermore, OMIEC-based artificial synapses have been demonstrated to show sensitivity to the composition of the ionic environment, arising from the interplay of dynamic noncovalent interactions between molecular solutes and OMIECs, which establishes the timescale of the neuromorphic response. This suggested the use of organic neuromorphic devices as sensors for species that exhibit an interaction with OMIECs stronger than that with ions in the electrolyte.

The aforementioned capability of performing specific discrimination of molecular signals in complex environments[84], as well as global connectivity control[85], multi-terminal operation[86], boolean logic implementation[87] and phase-dependent synchronicity[88] demonstrated how organic neuromorphic units can be integrated in efficient and functional “connectomes”. These features make connectomes suitable for recognizing signal patterns upon a supervised learning program. The single neuromorphic unit

response timescale[71] and amplitude can be reversibly tuned and coupled to amplification capability, thus enabling the design of a functional organic neuromorphic platform that can be promptly interfaced with living matter.[89] Neural probes do not benefit from these attractive features yet: if, on one hand, EGOT technology has been used for *in vivo* signal amplification[16,90], on the other hand demonstration of neuromorphic behavior is limited to the benchside or *in vitro*, and has not yet been demonstrated *in vivo*.

The features of OMIECs made them the most attractive materials for neuromorphic architectures, especially when compared to silicon-based devices[91].

1.8 Organic neuromorphic devices

The first report of neuromorphic behavior in organic electronic devices was achieved by the NOMFET (Nanoparticle Organic Memory Field Effect Transistor) architecture[92]. NOMFETs feature an operational principle which is different from that of the OMIEC-based neuromorphic devices used in this thesis, and are here briefly discussed solely to highlight their seminal importance in the development of organic neuromorphic electronics and to emphasize the key elements necessary for eliciting neuromorphic response in OE.

In particular, in OMIEC-based devices, the slow kinetic phenomenon necessary to elicit a neuromorphic response is inherent to the ion displacement in the electrolyte at the interface with the active layer, while in NOMFETs (figure 1.14a), the slow kinetic is obtained by embedding gold nanoparticles that act as shallow traps in an organic semiconductor thin film (pentacene). This device can mimic Short-Term-Plasticity (STP) of the drain-source current, acting as synaptic current, exhibiting facilitating or depressing behavior, by proper programming of the gate voltage acting as synaptic weight (figure 1.14 b,c).

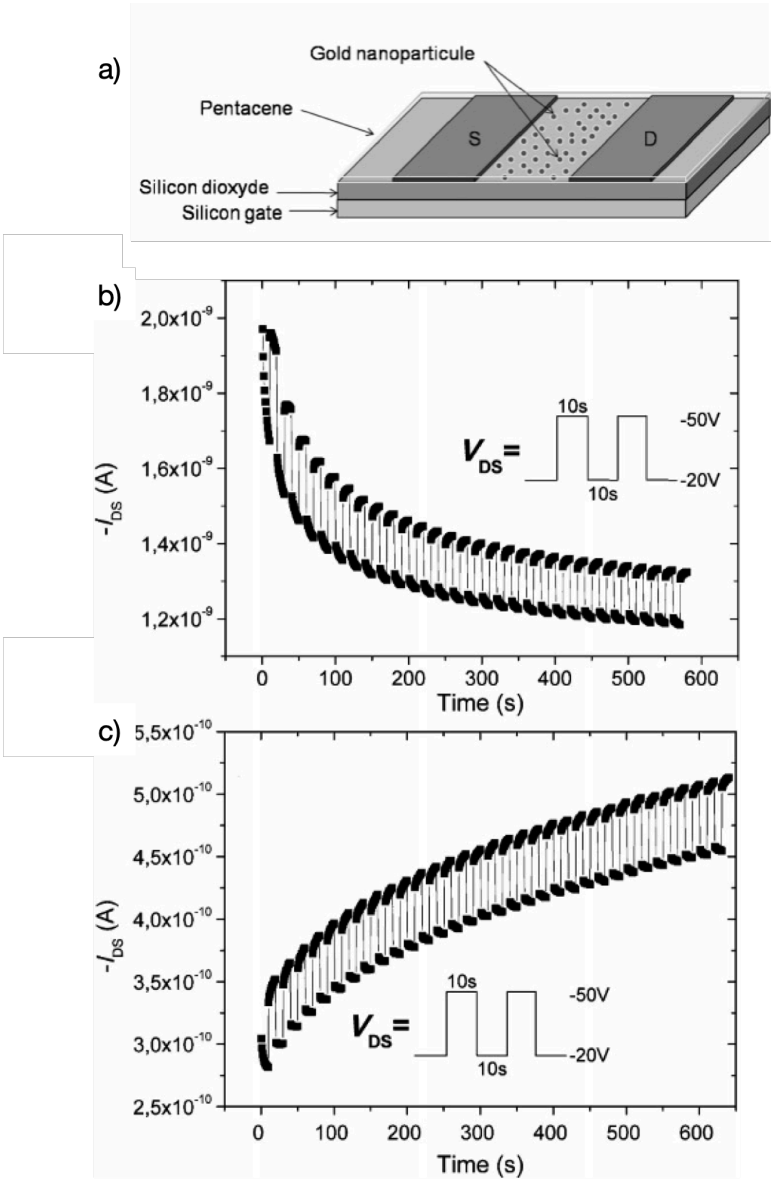

Figure 1.14 a) NOMFET device structure. b) Current NOMFET response applying gate voltage of -50 V. c) Current NOMFET response applying gate voltage of 50 V. The depressing or facilitating behavior depends both the duration between the pulses and the amount of charge trapped into the NPs. Figure from: *Alibart et al., Adv. Mat., 2010*[92].

To predict the performance of the NOMFET, Bichler et al. performed a simulation in Verilog-A language and implemented on Cadence Virtuoso platform with Spectre 5.1.41 simulator[93].

A similar study has been carried out on NOMFET using a polymer called Polyera™ N2200 with embedded gold NPs [94]. The STP response can be tuned in function of the pulse frequency applied, the channel length and the diameter of NPs.

Desbief et al.[95] developed a different kind of NOMFET, with OTS (Octadecyltricholorosilane) functionalization treatment, able to work with lower voltage amplitude. Comparing the results with the work by Vuillaume et al.[92], the same trend is obtained using an amplitude voltage of -1 V instead of -10 V.

Starting from these seminal results, such architectures have been widely modified and adapted to a vast application scenario. In particular, they have been integrated with cultured neural cells with neither loss of functionality nor impairment of cell viability[89], leading to the demonstration of the first bio-hybrid synapses[96]. They have been used as specific (bio-)sensors even without being endowed with specific bio-recognition groups (such as enzymes[97], antibodies[98], or aptamers[99]) to discriminate dopamine (DA) (a cation at physiological pH) not only from its antagonists in electrochemical assays[84] but also from its metabolites and catabolites[100] which differ from DA by a single functional group. In such application, quantification of the relevant molecule is inferred from the change of the time constant of depressive STP elicited in an OMIEC-based artificial synapse upon a 500 Hz stimulation.

The sensing mechanism is due to a strong interaction between DA and the employed OMIEC (in these cases PEDOT:PSS), which can be considered as resulting from two components: namely i) a π−π interaction between the aromatic rings of PEDOT:PSS and the DA catechol group and ii) a cation−π interaction between the ammonium group of DA and PEDOT:PSS. This strong interaction causes a delay in the recovery of the unperturbed state after spike removal, hence modulating the time constant.

Translating these proof-of-concept to *in vivo* would be important for in situ real-time detection of DA that may, in perspective, pave the way to loco-regional treatments of neurodegenerative conditions like Parkinson's disease.

References

1. Zhang, X., Bäuerle, P., Aida, T., Skabara, P. & Kagan, C. Organic Electronics for a Better Tomorrow : Innovation , Accessibility , Sustainability. *A White Pap. from Chem. Sci. Soc. Summit* 34 (2012).
2. Salehi, A., Fu, X., Shin, D. H. & So, F. Recent Advances in OLED Optical Design. *Adv. Funct. Mater.* **29**, 1–21 (2019).
3. Takeda, Y. *et al.* Fabrication of Ultra-Thin printed organic TFT CMOS logic circuits optimized for low-voltage wearable sensor applications. *Sci. Rep.* **6**, 1–9 (2016).
4. NanoMarkets. An opportunity analysis for OLED lighting: 2009 to 2016. *NanoMarkets* 1–13 (2009).
5. Yang, Y., Yang, X., Tan, Y. & Yuan, Q. Recent progress in flexible and wearable bio-electronics based on nanomaterials. *Nano Res.* **10**, 1560–1583 (2017).
6. Jang, J. Ultrasensitive Flexible Graphene Based Field-E ff ect Transistor (FET)-Type Bioelectronic Nose. (2012).
7. Bai, L. *et al.* Biological applications of organic electrochemical transistors: Electrochemical biosensors and electrophysiology recording. *Front. Chem.* **7**, 1–16 (2019).
8. Green, R. A. *et al.* Performance of conducting polymer electrodes for stimulating neuroprosthetics. *J. Neural Eng.* **10**, (2013).
9. Lee, W. & Someya, T. Emerging Trends in Flexible Active Multielectrode Arrays. *Chem. Mater.* **31**, 6347–6358 (2019).
10. Rivnay, J. *et al.* High-performance transistors for bioelectronics through tuning of channel thickness. *Sci. Adv.* **1**, 1–6 (2015).
11. Spyropoulos, G. D., Gelinas, J. N. & Khodagholy, D. Internal ion-gated organic electrochemical transistor: A building block for integrated bioelectronics. *Sci. Adv.* **5**, eaau7378 (2019).
12. Bettinger, C. J. Advances in Materials and Structures for Ingestible Electromechanical Medical Devices. *Angew. Chemie - Int. Ed.* **57**, 16946–16958 (2018).
13. Won, S. M. *et al.* Recent Advances in Materials, Devices, and Systems for Neural Interfaces. *Adv. Mater.* **30**, 1–19 (2018).

14. Gu, X. *et al.* Organic Electrochemical Transistor Arrays for In Vitro Electrophysiology Monitoring of 2D and 3D Cardiac Tissues. *Adv. Biosyst.* **3**, 1–8 (2019).
15. Khodagholy, D. *et al.* In vivo recordings of brain activity using organic transistors. *Nat. Commun.* **4**, 1575 (2013).
16. Khodagholy, D. *et al.* NeuroGrid: Recording action potentials from the surface of the brain. *Nat. Neurosci.* **18**, 310–315 (2015).
17. Campana, A., Cramer, T., Simon, D. T., Berggren, M. & Biscarini, F. Electrocardiographic recording with conformable organic electrochemical transistor fabricated on resorbable bioscaffold. *Adv. Mater.* **26**, 3874–3878 (2014).
18. Tee, B. C. K., Wang, C., Allen, R. & Bao, Z. An electrically and mechanically self-healing composite with pressure- and flexion-sensitive properties for electronic skin applications. *Nat. Nanotechnol.* **7**, 825–832 (2012).
19. Ramuz, M., Tee, B. C. K., Tok, J. B. H. & Bao, Z. Transparent, optical, pressure-sensitive artificial skin for large-area stretchable electronics. *Adv. Mater.* **24**, 3223–3227 (2012).
20. Pang, C. *et al.* Highly skin-conformal microhairy sensor for pulse signal amplification. *Adv. Mater.* **27**, 634–640 (2015).
21. Kim, J. *et al.* Stretchable silicon nanoribbon electronics for skin prosthesis. *Nat. Commun.* **5**, 1–11 (2014).
22. Wang, X., Gu, Y., Xiong, Z., Cui, Z. & Zhang, T. Silk-molded flexible, ultrasensitive, and highly stable electronic skin for monitoring human physiological signals. *Adv. Mater.* **26**, 1336–1342 (2014).
23. Kim, S. Y. *et al.* Highly Sensitive and Multimodal All-Carbon Skin Sensors Capable of Simultaneously Detecting Tactile and Biological Stimuli. *Adv. Mater.* **27**, 4178–4185 (2015).
24. Kim, T. Il *et al.* Injectable, cellular-scale optoelectronics with applications for wireless optogenetics. *Science (80-.).* **340**, 211–216 (2013).
25. Jeon, J., Lee, H. B. R. & Bao, Z. Flexible wireless temperature sensors based on Ni microparticle-filled binary polymer composites. *Adv. Mater.* **25**, 850–855 (2013).
26. Chen, L. Y. *et al.* Continuous wireless pressure monitoring and mapping with ultra-small passive sensors for health monitoring and critical care. *Nat. Commun.* **5**, 1–10 (2014).

27. Kim, K. H., Oh, Y. & Islam, M. F. Graphene coating makes carbon nanotube aerogels superelastic and resistant to fatigue. *Nat. Nanotechnol.* **7**, 562–566 (2012).
28. Inal, S., Rivnay, J., Suiu, A. O., Malliaras, G. G. & McCulloch, I. Conjugated Polymers in Bioelectronics. *Acc. Chem. Res.* **51**, 1368–1376 (2018).
29. Someya, T., Bao, Z. & Malliaras, G. G. The rise of plastic bioelectronics. *Nature* **540**, 379–385 (2016).
30. Simon, D. T., Gabrielsson, E. O., Tybrandt, K. & Berggren, M. Organic Bioelectronics: Bridging the Signaling Gap between Biology and Technology. *Chem. Rev.* **116**, 13009–13041 (2016).
31. Paulsen, B. D., Tybrandt, K., Stavrinidou, E. & Rivnay, J. Organic mixed ionic–electronic conductors. *Nat. Mater.* (2019). doi:10.1038/s41563-019-0435-z
32. Khodagholy, D. *et al.* Organic electronics for high-resolution electrocorticography of the human brain. *Sci. Adv.* **2**, (2016).
33. Simon, D. T. *et al.* An organic electronic ion pump to regulate intracellular signaling at high spatiotemporal resolution. *TRANSDUCERS 2009 - 15th Int. Conf. Solid-State Sensors, Actuators Microsystems* 1790–1793 (2009). doi:10.1109/SENSOR.2009.5285721
34. Keene, S. T., Gkoupidenis, P. & Burgt, Y. van de. *Neuromorphic computing systems based on flexible organic electronics*. *Organic Flexible Electronics* (LTD, 2021). doi:10.1016/b978-0-12-818890-3.00018-7
35. Bronstein, H., Nielsen, C. B., Schroeder, B. C. & McCulloch, I. The role of chemical design in the performance of organic semiconductors. *Nat. Rev. Chem.* **4**, 66–77 (2020).
36. Chen, J., Tee, C. K., Shtein, M., Martin, D. C. & Anthony, J. Controlled solution deposition and systematic study of charge-transport anisotropy in single crystal and single-crystal textured TIPS pentacene thin films. *Org. Electron.* **10**, 696–703 (2009).
37. Marquez, A. V., McEvoy, N. & Pakdel, A. Organic Electrochemical Transistors (OECTs) Toward Flexible and Wearable Bioelectronics. *Molecules* **25**, 1–25 (2020).
38. Horowitz, B. G. Organic Field-Effect Transistors. 365–377 (1998).
39. Wang, D., Noël, V. & Piro, B. Electrolytic gated organic field-effect transistors for application in biosensors—A review. *Electronics* **5**, (2016).
40. Casalini, S., Leonardi, F., Cramer, T. & Biscarini, F. Organic field-effect transistor

for label-free dopamine sensing. *Org. Electron.* **14**, 156–163 (2013).

41. Charles R Noback, David A Ruggiero, Robert J Demarest, N. L. S. *The Human Nervous System - Structure and Function*. (2005).
42. Kim, M. K., Park, Y., Kim, I. J. & Lee, J. S. Emerging Materials for Neuromorphic Devices and Systems. *iScience* **23**, 101846 (2020).
43. Kakoty, N. M., Kaiborta, M. & Hazarika, S. M. Electromyographic Grasp Recognition for a Five Fingered Robotic Hand. *IAES Int. J. Robot. Autom.* **2**, 1 (2012).
44. Yu, L. & Yu, Y. Energy-efficient neural information processing in individual neurons and neuronal networks. *J. Neurosci. Res.* **95**, 2253–2266 (2017).
45. Berlucchi, G. & Buchtel, H. A. Neuronal plasticity: Historical roots and evolution of meaning. *Exp. Brain Res.* **192**, 307–319 (2009).
46. Kelley, P. & Whatson, T. Making long-term memories in minutes: A spaced learning pattern from memory research in education. *Front. Hum. Neurosci.* **7**, 1–9 (2013).
47. Hughes, R. Potentiation. (1958).
48. Fioravante, D. & Regehr, W. G. Short-term forms of presynaptic plasticity. *Curr. Opin. Neurobiol.* **21**, 269–274 (2011).
49. Zucker, R. S. & Regehr, W. G. Short-term synaptic plasticity. *Annu. Rev. Physiol.* **64**, 355–405 (2002).
50. L.F. Abbott & Wade G. Regehr. Synaptic computation. *Results Math.* (2004). doi:10.1007/s00025-018-0858-x
51. Natschläger, T., Maass, W. & Zador, A. Efficient temporal processing with biologically realistic dynamic synapses. *Netw. Comput. Neural Syst.* **12**, 75–87 (2001).
52. Zador, A. Impact of synaptic unreliability on the information transmitted by spiking neurons. *J. Neurophysiol.* **79**, 1219–1229 (1998).
53. Baddeley, A. & Hitch, G. Working Memory. *Med. Res. Counc.* 47–88 (1974).
54. Wang, X. J. Decision Making in Recurrent Neuronal Circuits. *Neuron* **60**, 215–234 (2008).
55. Deng, P. Y. & Klyachko, V. A. The diverse functions of short-term plasticity components in synaptic computations. *Commun. Integr. Biol.* **4**, 543–548 (2011).
56. McCulloch, W. S. & Pitts, W. A logical calculus of the ideas immanent in nervous activity (reprinted from bulletin of mathematical biophysics, vol 5, pg 115-133,

1943). *Bull. Math. Biol.* **52**, 99–115 (1990).

57. Hodgkin, A. L. & Huxley, A. F. The components of membrane conductance in the giant axon of Loligo. *J. Physiol.* **116**, 473–496 (1952).
58. Rosenblatt, F. The Perceptron - A Perceiving and Recognizing Automaton. *Report 85, Cornell Aeronautical Laboratory* 460–1 (1957).
59. Bre, F., Gimenez, J. M. & Fachinotti, V. D. Prediction of wind pressure coefficients on building surfaces using artificial neural networks. *Energy Build.* **158**, 1429–1441 (2018).
60. Haffner, Y. L. L. B. Y. B. P. Gradient-Based Learning Applied to Document Recognition. *Proc. IEEE* **86**, (1998).
61. Pacheco, P. *An Introduction to Parallel Programming*. *An Introduction to Parallel Programming* (2011). doi:10.1016/C2009-0-18471-4
62. Carver Mead. Neuromorphic Electronic Systems. *Proc. IEEE* **78**,
63. Carver, M. & Ismail, M. *Analog VLSI Implementation of Neural Systems*. (Kluwer Academic Publishers, 1989).
64. Tuchman, Y. *et al.* Organic neuromorphic devices: Past, present, and future challenges. *MRS Bull.* **45**, 619–630 (2020).
65. Van De Burgt, Y., Melianas, A., Keene, S. T., Malliaras, G. & Salleo, A. Organic electronics for neuromorphic computing. *Nat. Electron.* **1**, 386–397 (2018).
66. Mead, C. Neuromorphic electronic systems. *Proc. IEEE* **78**, 1629–1636 (1990).
67. McDonnell, M. D., Boahen, K., Ijspeert, A. & Sejnowski, T. J. Engineering intelligent electronic systems based on computational neuroscience [scanning the issue]. *Proc. IEEE* **102**, 646–651 (2014).
68. Van De Burgt, Y. *et al.* A non-volatile organic electrochemical device as a low-voltage artificial synapse for neuromorphic computing. *Nat. Mater.* **16**, 414–418 (2017).
69. Gkoupidenis, P., Schaefer, N., Garlan, B. & Malliaras, G. G. Neuromorphic Functions in PEDOT:PSS Organic Electrochemical Transistors. *Adv. Mater.* **27**, 7176–7180 (2015).
70. Hu, Y. *et al.* Diverse Synaptic Plasticity Induced by the Interplay of Ionic Polarization and Doping at Salt-Doped Electrolyte/Semiconducting Polymer Interface. *ACS Omega* **2**, 746–754 (2017).
71. Di Lauro, M. *et al.* Tunable Short-Term Plasticity Response in Three-Terminal Organic Neuromorphic Devices. *ACS Appl. Electron. Mater.* **2**, 1849–1854 (2020).

72. Chang, T., Jo, S. H. & Lu, W. Short-term memory to long-term memory transition in a nanoscale memristor. *ACS Nano* **5**, 7669–7676 (2011).
73. Wang, Z. *et al.* Memristors with diffusive dynamics as synaptic emulators for neuromorphic computing. *Nat. Mater.* **16**, 101–108 (2017).
74. Liu, G. *et al.* Organic Biomimicking Memristor for Information Storage and Processing Applications. *Adv. Electron. Mater.* **2**, 1–8 (2016).
75. Lapkin, D. A., Emelyanov, A. V., Demin, V. A., Berzina, T. S. & Erokhin, V. V. Spike-timing-dependent plasticity of polyaniline-based memristive element. *Microelectron. Eng.* **185**–**186**, 43–47 (2018).
76. Lai, Q. *et al.* Ionic/electronic hybrid materials integrated in a synaptic transistor with signal processing and learning functions. *Adv. Mater.* **22**, 2448–2453 (2010).
77. Masquelier, T., Guyonneau, R. & Thorpe, S. J. Competitive STDP-based spike pattern learning. *Neural Comput.* **21**, 1259–1276 (2009).
78. Abbott, L. F. & Nelson, S. B. Nn1100_1178. *Nat. Neurosci.* **3**, 1178–1183 (2000).
79. Lynch, M. A. Long-Term Potentiation and Memory. *Physiol. Rev.* **84**, 87–136 (2004).
80. Caporale, N. & Dan, Y. Spike timing-dependent plasticity: A Hebbian learning rule. *Annu. Rev. Neurosci.* **31**, 25–46 (2008).
81. Mcelroy, M. B. *et al.* Synapse Modification. *Office* **237**, 42–48 (1986).
82. Keene, S. T., Melianas, A., van de Burgt, Y. & Salleo, A. Mechanisms for Enhanced State Retention and Stability in Redox-Gated Organic Neuromorphic Devices. *Adv. Electron. Mater.* **5**, 1–10 (2019).
83. Fuller, E. J.; Keene, S. T.; Melianas, A.; Wang, Z.; Agarwal, S.; Li, Y.; Tuchman, Y.; James, C. D.; Marinella, M. J.; Yang, J. J. . et al. Parallel Programming of an Ionic Floating-Gate Memory Array for Scalable Neuromorphic Computing. **364**, 570–574 (2019).
84. Giordani, M. *et al.* Specific Dopamine Sensing Based on Short-Term Plasticity Behavior of a Whole Organic Artificial Synapse. *ACS Sensors* **2**, 1756–1760 (2017).
85. Gkoupidenis, P., Koutsouras, D. A. & Malliaras, G. G. Neuromorphic device architectures with global connectivity through electrolyte gating. *Nat. Commun.* **8**, 1–8 (2017).
86. Gkoupidenis, P., Koutsouras, D. A., Lonjaret, T., Fairfield, J. A. & Malliaras, G. G. Orientation selectivity in a multi-gated organic electrochemical transistor. *Sci.*

Rep. **6**, 1–6 (2016).

87. Perez, J. C. & Shaheen, S. E. Neuromorphic-based Boolean and reversible logic circuits from organic electrochemical transistors. *MRS Bull.* **45**, 649–654 (2020).
88. Koutsouras, D. A., Prodromakis, T., Malliaras, G. G., Blom, P. W. M. & Gkoupidenis, P. Functional Connectivity of Organic Neuromorphic Devices by Global Voltage Oscillations. *Adv. Intell. Syst.* **1**, 1900013 (2019).
89. Desbief, S. *et al.* Electrolyte-gated organic synapse transistor interfaced with neurons. *Org. Electron.* **38**, 21–28 (2016).
90. Cea, C. *et al.* Enhancement-mode ion-based transistor as a comprehensive interface and real-time processing unit for in vivo electrophysiology. *Nat. Mater.* (2020). doi:10.1038/s41563-020-0638-3
91. Lee, Y. & Lee, T. W. Organic Synapses for Neuromorphic Electronics: From Brain-Inspired Computing to Sensorimotor Nervetronics. *Acc. Chem. Res.* **52**, 964–974 (2019).
92. Alibart, F. *et al.* An organic nanoparticle transistor behaving as a biological spiking synapse. *Adv. Funct. Mater.* **20**, 330–337 (2010).
93. Bichler, O. *et al.* Functional model of a nanoparticle organic memory transistor for use as a spiking synapse. *IEEE Trans. Electron Devices* **57**, 3115–3122 (2010).
94. Hafsi, B. *et al.* Electron-transport polymeric gold nanoparticles memory device, artificial synapse for neuromorphic applications. *Org. Electron.* **50**, 499–506 (2017).
95. Desbief, S. *et al.* Low voltage and time constant organic synapse-transistor. *Org. Electron. physics, Mater. Appl.* **21**, 47–53 (2015).
96. Keene, S. T. *et al.* A biohybrid synapse with neurotransmitter-mediated plasticity. *Nat. Mater.* **19**, 969–973 (2020).
97. Berto, M. *et al.* Label free urea biosensor based on organic electrochemical transistors. *Flex. Print. Electron.* **3**, (2018).
98. Berto, M. *et al.* Biorecognition in organic field effect transistors biosensors: The role of the density of states of the organic semiconductor. *Anal. Chem.* **88**, 12330–12338 (2016).
99. Berto, M. *et al.* EGOFET Peptide Aptasensor for Label-Free Detection of Inflammatory Cytokines in Complex Fluids. *Adv. Biosyst.* **1700072**, 1700072 (2017).
100. Giordani, M. *et al.* Neuromorphic Organic Devices that Specifically Discriminate

Dopamine from Its Metabolites by Nonspecific Interactions. *Adv. Funct. Mater.* **30**, 2002141 (2020).

2. Aim and strategy

The aim of this thesis is to investigate the fundamental and translational aspects of the neuromorphic Short-Term Plasticity (STP) response in organic electronic devices by tuning their characteristic time–scale. This investigation is focused mainly on two device categories:

- Three-terminal devices (i.e. Electrolyte-Gated Organic Transistors – EGOTs), in which the peculiar features of EGOTs are used to develop a new class of organic neuromorphic devices exhibiting reversibly tunable Short-Term Plasticity (STP) response of the channel current;

- Two-terminal implantable organic artificial synapses, built on intracortical microelectrodes, exhibiting frequency modulation of the STP response and showing a frequency-dependent crossover between depressive and facilitative behavior.

For both device categories, analytical models have been developed, reaching a comprehensive theoretical platform towards the explanation of the physical origin of STP and of its timescales in terms of charge build up in PEDOT/PSS, allowing quantitative description of transient phenomena in organic neuromorphic bioelectronics.

Concerning the translational aspects, this thesis is centered on two main goals:

- To explore the tunability of the neuromorphic response in organic transistors aiming to tailorable functional units for organic artificial neural networks;

- To devise strategies for performing *in vivo* bio-sensing with implantable organic artificial synapses, focusing on dopamine detection and quantification firstly in vitro and up to in vivo scenarios.

3. Tunable STP in EGOTs

This chapter reports on the development of three-terminal architectures, namely Electrolyte-Gated-Organic-Transistors (EGOTs) in accumulation and depletion mode, exhibiting tunable short-term plasticity. The materials, methods, steady state and transient neuromorphic characterization of EGOTs are discussed in this section. This activity led to the publication of the article: "*ACS Appl. Electron. Mater.* 2020, 2, 7, 1849–1854"

3.1 Materials and Method

3.1.1 Depletion EGOTs fabrication

Custom test patterns were designed and purchased by Phoenix PCB (Ivrea, Italy). The final design (Figure 3.1a) features nine independent pairs of gold Source/Drain electrodes (W/L=4) patterned onto a flexible poly-imide substrate. Insulation is guaranteed by a further poly-imide layer which covers the entire layout and features nine pools which expose only the terminal portion (area = 0.8mm x 0.9mm) of the Source and Drain leads. Semiconductive channels are obtained by drop-casting 0.5 µL of a PEDOT:PSS formulation (Clevios PH1000, 5% v/v DMSO, 0.2% v/v GOPS; diluted ten times with MilliQ water) on each pool (Figure 3.1b) and curing in a thermostatic oven (120°C, 30 min) obtaining films with an average 1 µm thickness (XE7 AFM Park System, tapping mode).

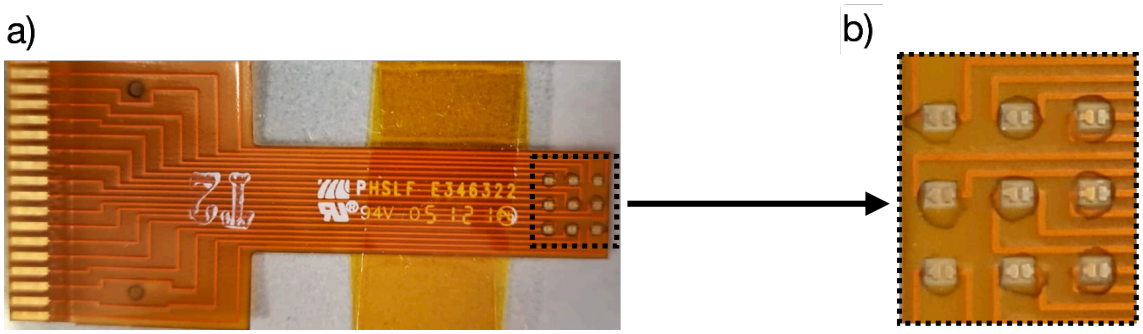

Figure 3.1 a) A matrix with a (b) zoom on the electrodes area.

3.1.2 Accumulation EGOTs fabrication

Gold Source and Drain interdigitated electrodes (W/L = 200) were deposited onto quartz substrates by photolithography and lift-off (MicroFabSolutions, Trento, Italy), obtaining a 15 µm long and 3 mm wide channel. The organic semiconductor 6,13-bis(triisopropylsilylethynyl)pentacene (TIPS-P5) was deposited, after piraña wet etch (1:1, H_2SO_4:H_2O_2) treatment onto these substrates, via spin coating of a 1% w/w solution in a 8:2 mixture of Toluene and n-Hexane and cured in a thermostatic oven (60°C, 30 min). This treatment carried out to the formation of TIPS-P5 crystals on the quartz glass substrate (Figure 3.2).

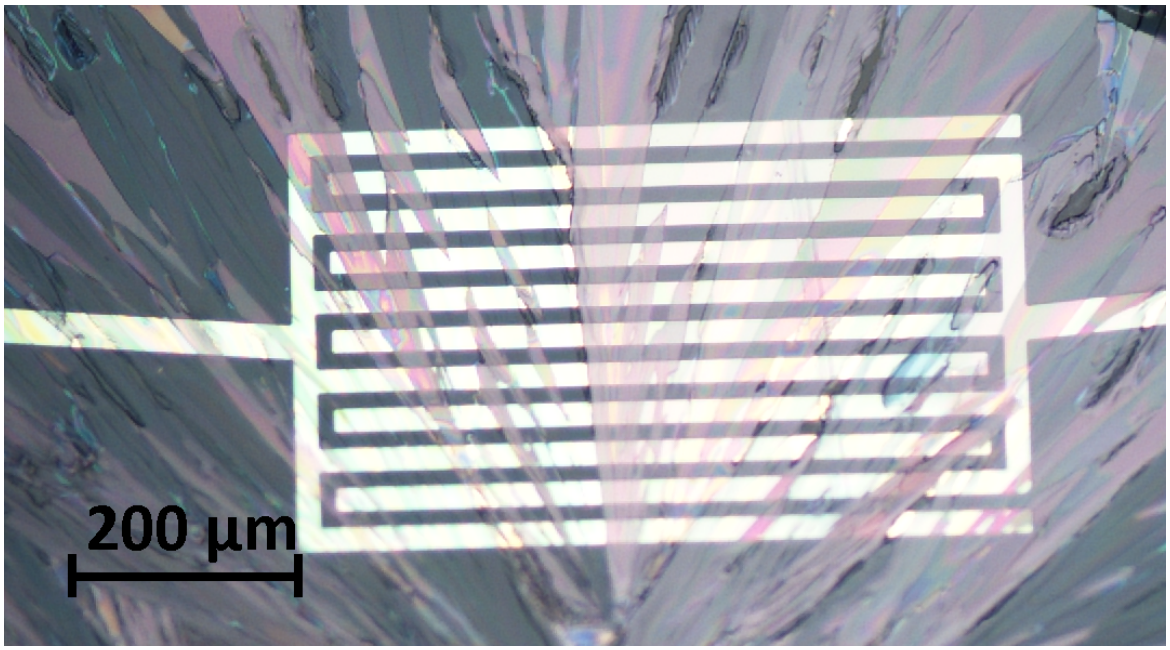

Figure 3.2 TIPS pentacene crystallization after deposition by spin-coating and curing in oven. Magnification of the crystalized interdigitation obtained by optical microscope.

3.1.3 EGOT electrical characterization

The electrical characterization of the devices presented in this thesis was performed with a Keysight B2912A Source-Measure-Unit (SMU), shown in Figure 3.3 a, that features two channels for independently sourcing voltage/current and measuring current/voltage. Each channel features 6 banana outputs, which are converted to two triaxial outputs (Low and High Force) by means of adapters, Figure 3.3 b; the low terminal can be grounded to the chassis of the instrument or left floating. A custom-designed software controls both channels of the SMU and allows tailoring of the measurement routine as well as data comparison, filtering and analysis. Figure 3.3 c shows an example of the graphical user interface of the software.

In particular, I-V characteristics have been acquired in the usual common Source-common Ground configuration while neuromorphic tunable behavior has been obtained driving the pulsed Drain electrode with one channel of the SMU, using the other channel to provide a DC bias at the Gate electrode.

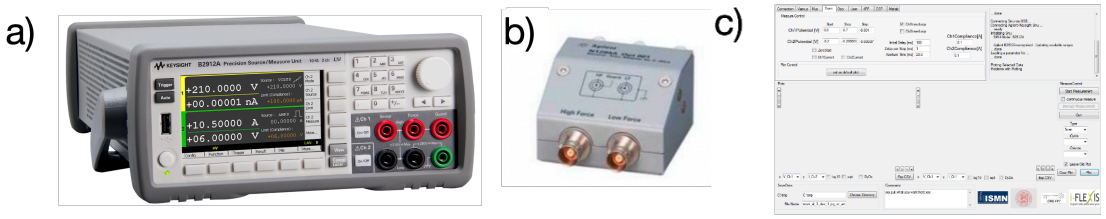

Figure 3.3 a) Agilent B2912A SMU; b) Agilent N1294A banana-to-triax adapters; c) scan interface of the SMU Control Software.

3.2 I-V EGOT characteristics

As a first step, the amplification capability of EGOT architecture are assessed by means of I-V characterization. In particular, the I−V transfer characteristics were performed by sweeping the gate-source voltage (V_{GS}) from 0.6 V to −0.6 V for depletion EGOTs, while (V_{GS}) from 0 V to −0.8 V for accumulation EGOTs, leaving the drain-source voltage (V_{DS}) constant at −0.6 V and -0.2, respectively. The outputs for depletion EGOTs were obtained by sweeping the V_{DS} from 0 V to -0.7 V for V_{GS} values from 0.6 V to -0.6 V stepped by 0.1 V; for accumulation EGOTs outputs were also obtained by sweeping the V_{DS} from 0 V to -0.8 V for V_{GS} value from 0 V to -0.8 V stepped by 0.2 V. All electrical measurements have been acquired in a buffer solution (PBS 50 mM, pH 7.4) in order to mimic physiological conditions and carried out in atmosphere conditions (temperature and humidity). I-V device performances are summarized in Figure 3.4.

Schematic representations of the depletion and accumulation EGOTs architectures, already discussed in the chapter 1, are reported in figure 3.4 a and b. Transfer (Figure 3.4.c and Figure 3.4.d) and output (Figure 3.4.e and Figure 3.4.f) characteristics confirmed that PEDOT:PSS - based EGOTs exhibit higher absolute I_{DS} values compared to TIPS-P5-based devices. Nevertheless, as shown in Figure 3.4.g and Figure 3.4.h, in both architectures is it possible to reversibly shift from a high-conductance state to a low-conductance state when scanning V_{GS} from negative to positive values; this common feature has been exploited to tune STP depressive response in both architectures.

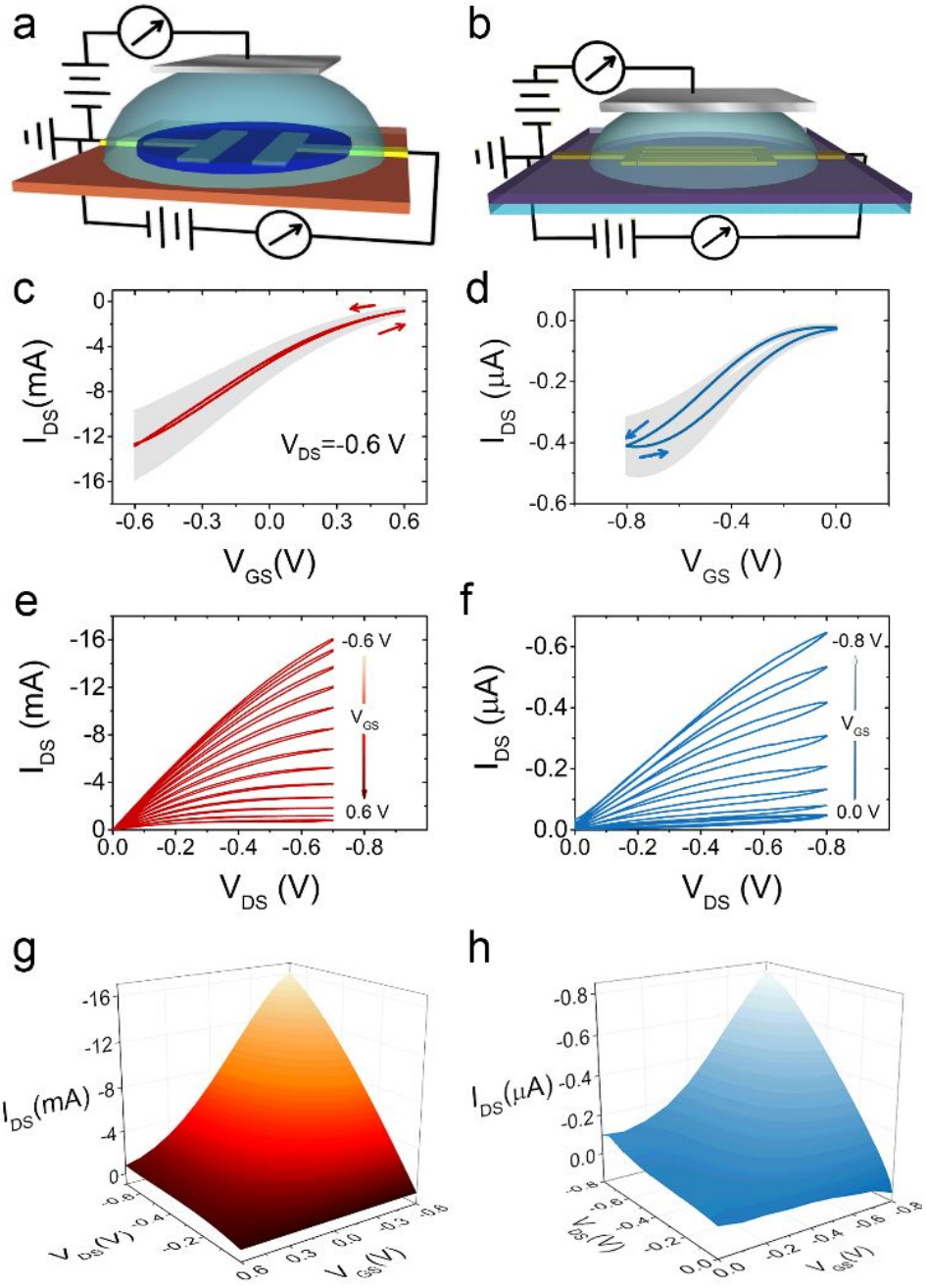

Figure 3.4 a-b) schematic representation and connection layout of the proposed PEDOT:PSS-based depletion EGOT (a) and TIPS-pentacene accumulation EGOT (b), operated in common source-common ground configuration; c-d) average transfer characteristics of depletion (c) and accumulation (d) devices, reported with their SEM (N=5, grey area); e-f) typical output characteristics of depletion (e) and accumulation (f) devices; g-h) 3-D plots showing the dependence of I_{DS} from both V_{GS} and V_{DS}, for depletion (g) and accumulation (h) devices.

3.3 Short-Term Plasticity response in Three-Terminal Organic Neuromorphic Devices

Usually, when organic transistor architectures are operated to yield neuromorphic response, two of the three terminals are short-circuited together, obtaining a *de facto* two-terminal architecture[1], whose time/frequency response reflects an effective RC time constant of the circuit. This time constant depends on geometrical features such as channel thickness[2], on the judicious integration of shallow traps, for instance made with Au nanoparticles as previousled for NOMFETs[3], or on the composition of the electrolyte or the presence of molecules strongly interacting with the active layer. In all these approaches depressive STP is obtained when the voltage spike train has a frequency higher than the inverse of the device response characteristic timescale, which is largely contributed by the resistance-capacitance of the electrolyte/active material interface.

In other three-terminal approaches[4–7], STP has been achieved in poly(3,4-ethylenedioxythiophene):polystyrene sulfonate (PEDOT:PSS)-based EGOTs by continuously recording I_{DS} while applying pulses at the Gate electrode and exploiting the rather slow bulk de-doping/doping of semi-conductive channels to achieve non-linearity of the I_{DS} response according to the stimulation frequency. LTP, on the other hand, has been achieved by faradaic processes such as lithium intercalation in the channel of graphene FETs[8], In this chapter, a novel EGOT-based neuromorphic architecture is reported, in which the doping state of the channel is kept constant throughout the entire stimulation protocol by applying a constant V_{GS}. An STP depressive response of I_{DS} is observed upon V_{DS} square pulsing, achieving selective and reversible tuning of STP behavior via V_{GS}-mediated control of channel doping. Importantly, the gate voltage does not produce any redox reaction in the active layer. The rationale is that eliciting STP-modulation of I_{DS} by square pulse V_{DS} stimulation it is possible to exploit V_{GS} as an

additional tuning parameter, to modulate charge carrier density in the semi-conductive channel, regulating both STP-amplitude and STP-time constant at the same time. The gate also allows the baseline current to be set before and at the steady state after the STP response, thus acting as a further element for memory writing. A schematic representation of the connection layout is presented in Figure 3.5.a.

The envisioned stimulation protocol was validated by sourcing square pulse-trains of varying frequencies at the drain electrode following an established stimulation pattern[9], while applying a constant DC bias V_{GS} at the gate and keeping a fixed non-zero drain bias ($V_{DS,0}$ = -0.3V). Figure 3.5 b shows the stimulation protocol and the response of a three-terminal STP device obtained in a depletion PEDOT:PSS-based EGOT: upon channel de-doping (i.e. when moving from negative V_{GS} values to positive ones) it is possible to observe a decrease of the current spikes amplitude. This is consistent with the profile of the transfer characteristics (shown in Figure 3.4.c), which is also mirrored by the trend of the DC current in absence of stimulation.

The typical response of neuromorphic two-terminal devices is qualitatively retained: it is possible to observe linear response at low frequencies, a depressive response at high frequencies and a facilitating response (*viz.* current spike amplitude increasing) when moving from high to low frequencies. Nonetheless, in three-terminal architecture, it is possible to modulate this behavior, at least until the neuromorphic response for completely de-doped channels (i.e. V_{GS} = 0.6 V) is suppressed. This behavior arises from the different nature of charge-carriers contributing to I_{DS} in response to V_{DS} pulses: namely, holes hopping in the semi-conductive channel (slow carriers) and ions displacing in the electrolyte (fast carriers). When the channel is completely de-doped, holes are trapped and I_{DS} is due to mere ion displacement, resulting in lower current intensity and faster relaxation time-scales. In this scenario the stimulation frequency is not high enough

to elicit depression, and device response will be linear. This effect is displayed in Figure 3.5.c, showing the current variations ΔI_{DS} in response to individual V_{DS} square waves in the "depressive" region. Besides the aforementioned decrease of intensity, it is possible to observe the significant evolution of the relaxation time-scales exhibited by the system when pulses are applied and removed. Interestingly, it is possible to decouple these two phenomena (pulse application and pulse removal) if no DC drain bias is applied (i.e. if $V_{DS,0} = 0$V), as shown in Figure 3.5.d.

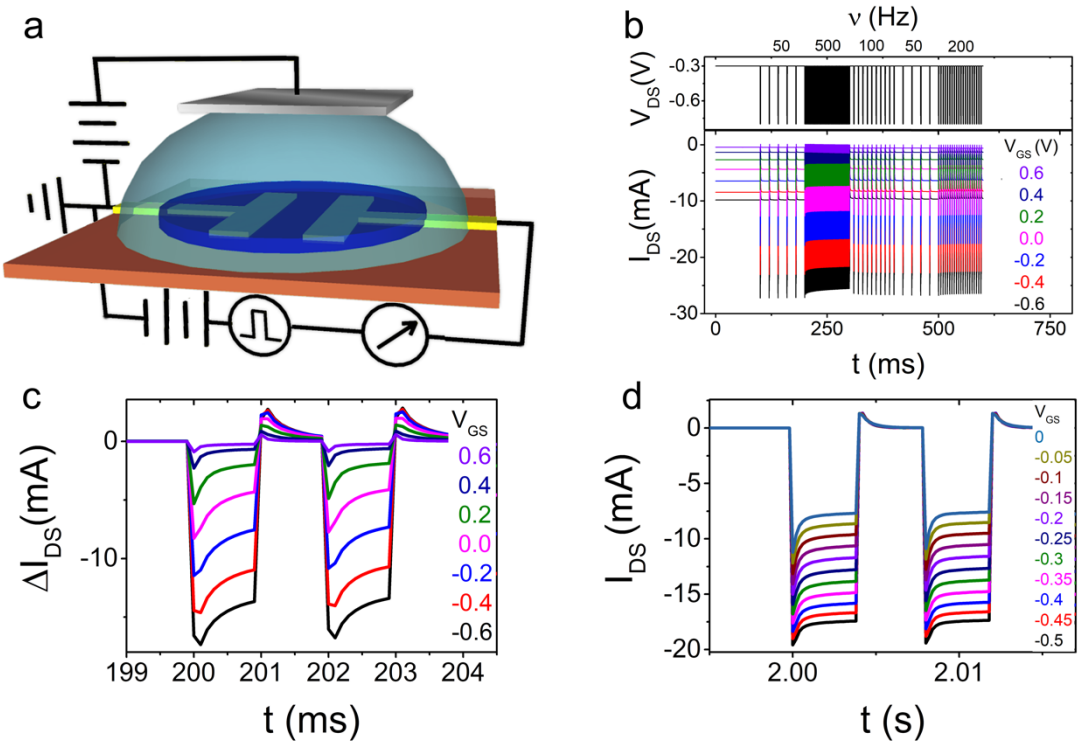

Figure 3.5 a) connection layout for eliciting tunable STP response: a constant Gate bias is applied while at the drain terminal voltage pulses are applied and I_{DS} is recorded; b) response of the accumulation EGOT to a V_{DS} pulse train ($V_{DS,0}$ = -0.3V; ΔV_{DS} = -0.5 V) at different V_{GS} values; c) detail of I_{DS} variations in the depressive region of (b) at 500 Hz, highlighting the dependency of both spike amplitude and relaxation timescales on V_{GS}; d) system response to depressive stimulation frequency (125 Hz) for $V_{DS,0} = 0$V, for -0.5 V < V_{GS} < 0 V.

In order to define operational parameters necessary for predicting and tailoring the STP response in a three-terminal device, it is necessary to develop a quantitative toolset that rationalizes these phenomena. In this work, this has been done by focusing on the STP depressive response at 125 Hz at $V_{DS,0}$ = 0V, for V_{GS} values ranging to 0 V to -0.5 V since, within this potential window, it is possible to modulate the conductivity of the large majority of *p*-type organic semi-conductors and is possible to rule out any faradaic contribution to the observed currents[10].

The typical STP depressive response, characterized by a decreasing envelope of the current maxima in response to subsequent voltage spikes (shown in Figure 3.6.a and 3.6.b), follows the stretched exponential trend of Equation 3.1:

$$I(t) = I_{\infty} + A \cdot exp\left[-\left(\frac{\Delta t}{\tau_{STP}}\right)^{\beta}\right] \quad (3.1)$$

where I_{∞} is the current plateau related to the equilibrium reached upon continuous depressive stimulation, $A = I_0 - I_{\infty}$ is the difference between the first spike, I_0 and I_{∞}, $\Delta t = t - t_0$ is the time interval from the first spike, τ_{STP} is the STP timescale and the exponent, β, quantifies the deviation from the exponential trend (which is instead usually observed in two-terminal devices)[11]. Figure 3.6.c shows the trends of I_{∞} and A vs V_{GS} for depletion EGOTs, while figure 3.6.d reports the same trends for accumulation devices. In depletion devices, the increasing trend of I_{∞} for higher channel doping (i.e. more negative V_{GS} and higher negative I_{∞}) is mirrored by a decrease in STP amplitude, A. This is due to the fact that, for negative V_{GS}, conduction in PEDOT:PSS approaches metallic conduction, resulting in a partial loss of tunability. In accumulation devices, on the other hand, the active material is completely undoped at $V_{GS} = 0$ and is populated of charge carriers while moving at more negative V_{GS}; in this situation the amplitude of the STP modulation, A, and the plateau current, I_{∞}, follow exactly the same trend vs V_{GS}. This shows that V_{GS} also controls current baseline.

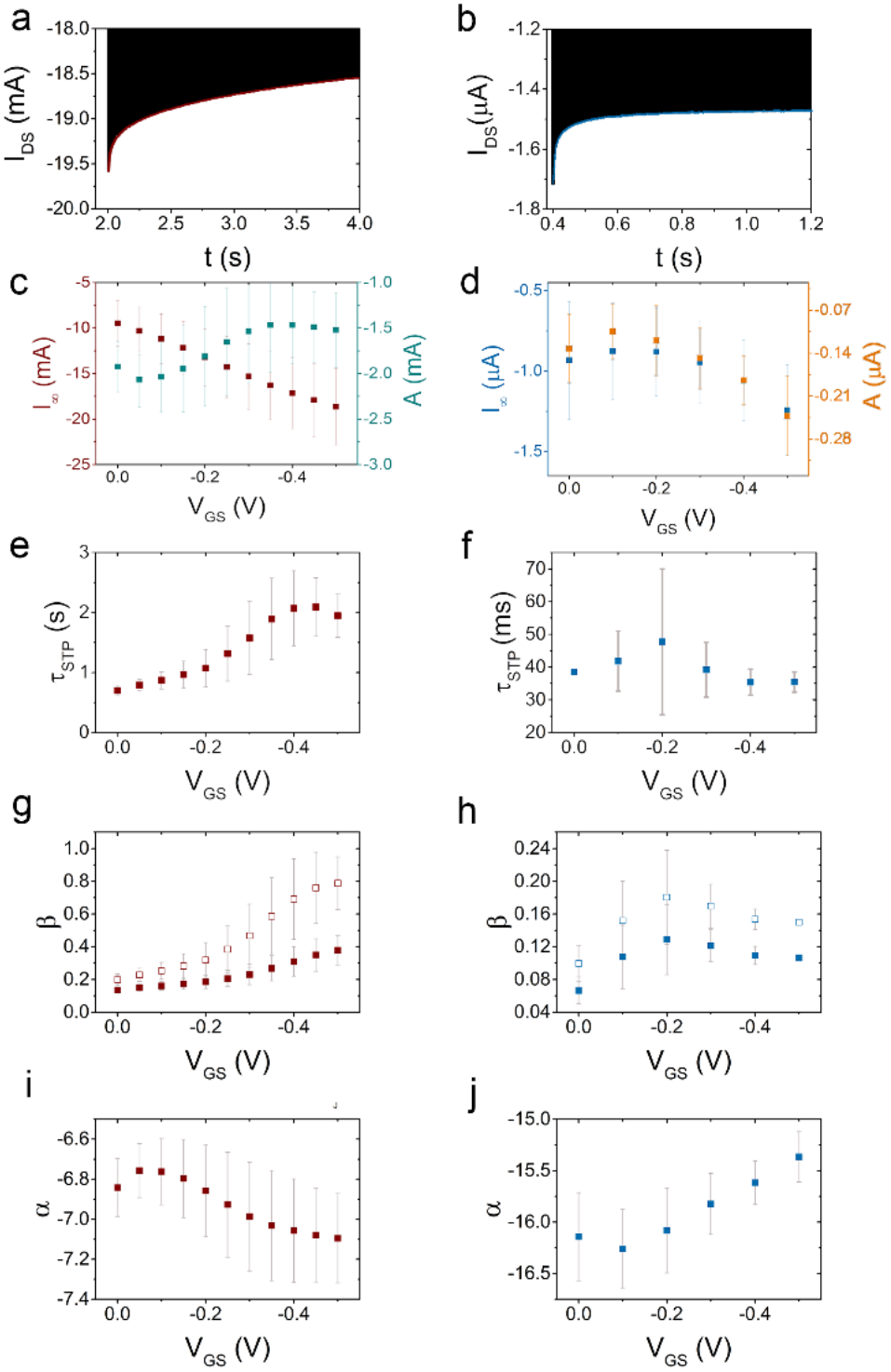

Figure 3.6 a-b) typical depressive STP-responses (solid black line) and STP-envelopes (solid red and blue lines) for depletion (a) and accumulation (b) devices; c-d) dependency of current plateau, I_∞, and STP amplitude, A, on V_{GS}, for depletion (c) and accumulation (d) devices; e-f) dependency of STP timescale, τ_{STP}, on V_{GS}, for depletion (e) and accumulation (f) devices; g-h) dependency of stretching exponent, β, as extracted from the stretched exponential trend (hollow squares) and from the linearized one (solid squares) on V_{GS}, for depletion (g) and accumulation (h) devices; i-j) dependency of the linearized trends slope, α, on V_{GS}, for depletion (i) and accumulation (j) devices.

The stretching exponent, β (plotted vs V_{GS} in Figure 3.6.g and Figure 3.6.h for depletion and accumulation devices, respectively), is a measure of the deviation from the ideal exponential STP decay. In the three-terminal architecture, the observed $\beta < 1$ produces a less steep decay. This hints to energetic disorder and dispersion of drift velocities in semiconductive channels and it is different from displacement-based STP in two-terminal architectures, where β=1. Also β dependency on V_{GS} differs for depletion and accumulation devices. In the former, it increases with channel doping and approaches unity, resulting in steeper decays; in the latter in increases linearly in the sub-threshold operational regime (-0.2 V < V_{GS} <0 V, where the channel gets populated) and remains rather constant in the linear accumulation regime.

Since the sampled time for a train of voltage pulses may be shorter than the STP time scale (in some instances this falls outside the range of experimental time that means the plateau of STP is not fully achieved for the duration of the pulse train), the estimated errors on the fitting parameters are large and the convergence requires a step-and-hold fitting procedure. Thus, we recast eq. 1 and perform its Taylor expansion into a power law:

$$I(t) \approx I_0 + I_\infty \cdot \left(\frac{\Delta t}{\tau_{STP}}\right)^{\beta} \tag{3.2}$$

which can be linearized as:

$$ln\left[\frac{I(t)-I_0}{1A}\right] = \left[ln\left(\frac{I_\infty}{1A}\right) - \beta \cdot ln\left(\frac{\tau_{STP}}{1s}\right)\right] + \beta \cdot ln\left(\frac{\Delta t}{1s}\right) = \alpha + \beta \cdot ln\left(\frac{\Delta t}{1s}\right) \tag{3.3}$$

Fit with Equation 3.3 is numerically robust, although the physical meaning of the parameters of equation 3.2 is not explicit as they are now entangled into the parameter α, which is plotted vs V_{GS} in Figure 3.6.i and Figure 3.6.j. Linearization procedure also leads to a slight underestimation of β values, as shown in Figure 3.6.g and 3.6.h.

As already discussed, both α and β can be tuned by controlling V_{GS}.

The parameter α, namely the value of $ln\left[\frac{\Delta I(t)}{1A}\right]$ after 1 s of continuous depressive stimulation, is a generic indicator of the efficiency of the STP depression. Indeed, in depletion devices α exhibits a maximum at V_{GS} close to 0 V, where the channel is in its most energetically disordered state (see also Figure 3.4.c for comparison). Accordingly, β is minimum in this potential window.

In accumulation EGOTs, Figure 3.6.j, the trend is exactly reversed, since these devices experience the opposite transition, i.e. from insulating to conductive, while moving towards negative V_{GS} values, thus their STP efficiency scales directly with the charge carrier density.

As a complementary information to this framework, it is worth noticing that τ_{STP} – namely the time constant of the I_{DS} decay upon depressive stimulation – is different than circuit RC time constant, τ, extracted from impedance spectroscopy. In particular, devices with faster relaxation (i.e. smaller τ) exhibit longer τ_{STP}. This is not surprising if one considers the fact that STP arises from incomplete relaxation of the system upon continuous spiking: namely, at a given stimulation frequency, in a system with smaller τ the intensity of the second spike will be closer to that of the first spike if compared to what would happen in a slower system (bigger τ), resulting in the need of more spikes (i.e. longer times) to reach a steady-state, causing a longer τ_{STP}.

References

1. Alibart, F. *et al.* An organic nanoparticle transistor behaving as a biological spiking synapse. *Adv. Funct. Mater.* **20**, 330–337 (2010).
2. Gerasimov, J. Y. *et al.* An Evolvable Organic Electrochemical Transistor for Neuromorphic Applications. *Adv. Sci.* **6**, 1–8 (2019).
3. Desbief, S. *et al.* Electrolyte-gated organic synapse transistor interfaced with neurons. *Org. Electron.* **38**, 21–28 (2016).
4. Gkoupidenis, P., Schaefer, N., Garlan, B. & Malliaras, G. G. Neuromorphic Functions in PEDOT:PSS Organic Electrochemical Transistors. *Adv. Mater.* **27**, 7176–7180 (2015).
5. Qian, C. *et al.* Artificial Synapses Based on in-Plane Gate Organic Electrochemical Transistors. *ACS Appl. Mater. Interfaces* **8**, 26169–26175 (2016).
6. Ling, H. *et al.* Electrolyte-gated transistors for synaptic electronics, neuromorphic computing, and adaptable biointerfacing. *Appl. Phys. Rev.* **7**, (2020).
7. Hu, Y. *et al.* Diverse Synaptic Plasticity Induced by the Interplay of Ionic Polarization and Doping at Salt-Doped Electrolyte/Semiconducting Polymer Interface. *ACS Omega* **2**, 746–754 (2017).
8. Sharbati, M. T., Du, Y., Torres, J., Ardolino, N. D. & Yun, M. Low-Power , Electrochemically Tunable Graphene Synapses for Neuromorphic Computing. **1802353**, 1–6 (2018).
9. Desbief, S. *et al.* Low voltage and time constant organic synapse-transistor. *Org. Electron.* **21**, 47–53 (2015).
10. Cramer, T. *et al.* Water-gated organic field effect transistors – opportunities for biochemical sensing and extracellular signal transduction. *J. Mater. Chem. B* **1**, 3728 (2013).

11. Giordani, M. *et al.* Neuromorphic Organic Devices that Specifically Discriminate Dopamine from Its Metabolites by Nonspecific Interactions. *Adv. Funct. Mater.* **30**, 1–13 (2020).

4. Implantable Organic Artificial Synapses

This chapter reports the development of implantable organic artificial synapses and the mathematical modeling of their STP response, exhibiting a frequency-dependent crossover between depressive and facilitative response. This study resulted in the publication of the paper: "*Adv. Electron. Mater.* **7**, 1–8 (2021)." Moreover, the performances of artificial synapses as dopamine sensors both in artificial Cerebrospinal Fluid (aCSF) and in vivo are investigated and reported, rationalizing the results in view of the developed analytical model.

4.1 Two terminals device for STP mimicking

Aim of this study is the development and the characterization of an artificial synapse layout, exhibiting either depressive or facilitative STP, implemented on an implantable technological platform. In particular, intracortical microelectrodes have been chosen due to their minimum invasiveness and to their capability to be employed in deep brain implants, with the long-term goal of locally quantifying dopamine in vivo thanks to the modification of STP timescales, as discussed in Chapter 1.

Towards this aim, deep-brain fiber microelectrodes[1], originally designed for stimulation and recording, were endowed with neuromorphic response by electrochemically coating their tips with PEDOT/PSS. This coating is usually aimed at reducing interface impedance and/or at increasing biocompatibility in neural applications[2–6]. Here, a further function, viz. the ability to exhibit STP, is demonstrated. In this investigation, STP of such newly developed artificial synapses is characterized by systematic variation of the input frequency across two orders of magnitude, unveiling a crossover from depressive (at high frequency input voltage pulses) to facilitative (at lower frequency input voltage pulses) STP responses. An equivalent circuit model is then proposed to rationalize the observed STP response, which shows how the introduction of an inductive component, in parallel with the usual RC circuit adopted for purely depressive STP, allows one to fit and predict STP signals and their crossover. For the first time, the inductance is used for explaining the neuromorphic response in OMIEC-based artificial synapses, which points to the role of charge build up inside the OMIEC as an ionic mechanism of control of the STP features.

4.2 Artificial synapses fabrication

The so-called Thomas electrodes are intracortical electrodes commonly used for neural recording. The electrode is composed by a metal core (alloy: Platinum (Pt) 95 %, Tungsten (W) 5 % covered by quartz glass. The inner alloy metal diameter is about 25 µm, the overall fiber diameter is about 80 µm. The overall fiber is 10 m and it is wrapped in a spool (figure 4.1, left).

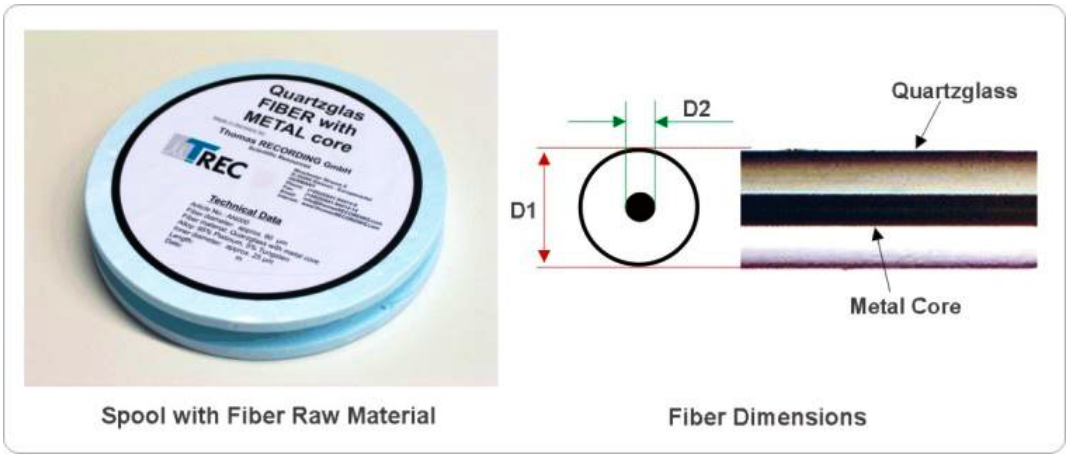

Figure 4.1 (left) Spool which wraps the overall electrode fiber of 10 m. (right) Technical parameters of electrode fiber: the diameter of whole fiber is about 80 µm (D1), the inner diameter is about 25 µm (D2).

The electrode tip grinding machine is constituted by a diamond disk, with a translation sledge for holding and rotating the electrode during the grinding (Figure 4.2. a,b); the sledge is adjustable for a tip angle up to 20 degrees. The tip is worked by two different engines. The first one sets in motion a diamond disk for tip elongation (Figure 4.2. c,d); the second one set in rotation the tip around itself to make it conical (Figure 4.2. e,f). A typical resultant finished tip is reported in the inset in figure 4.6 a.

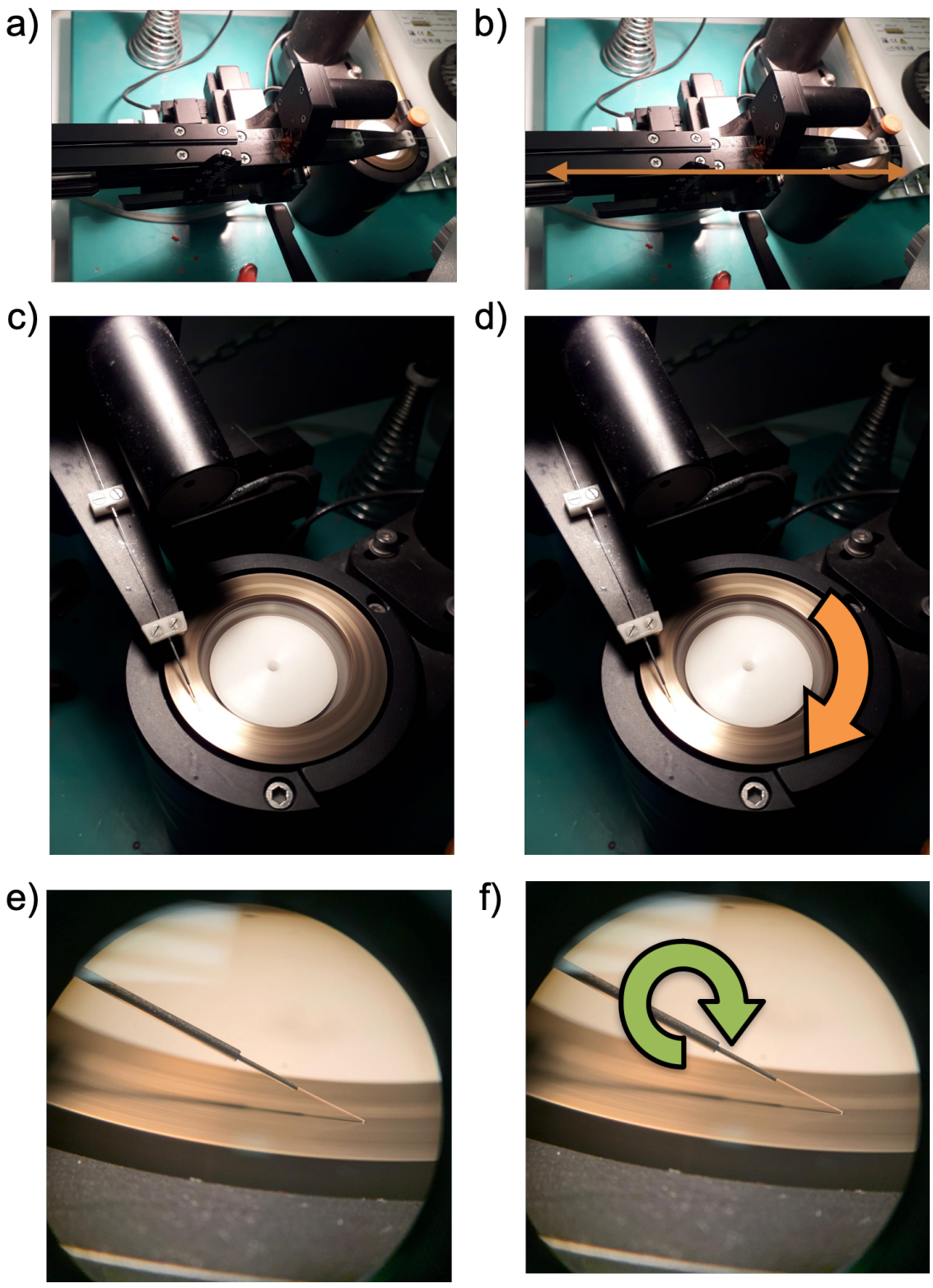

Figure 4.2 a) Electrode tip grinding machine DIECKL-ST; b) Insertion of the electrode fraction into the translation sledge; c,d) diamond disk for the tip electrode elongation; e,f) optical microscope image of the tip during the conicalization.

4.3 System design and characterization

As expected, the electrochemical deposition of PEDOT/PSS (blue film in the schematic drawing, (inset figure 4.6 a) by cronocoulometric technique (Figure 4.3 a) yields a significant reduction of the impedance |Z| in comparison to the bare Pt:W microelectrode (Figure 4.3 b).

PEDOT/PSS electrodeposition was carried out, according to published protocols[7–9], from an aqueous solution of EDOT (3,4-Ethylenedioxythiophene, 10×10^{-3} M) and NaPSS (sodium polystyrene sulfonate, 0.7% w/w) in potentiostatic mode (1 V vs Ag|AgCl; 5 s pre-conditioning step: 0.2 V vs Ag|AgCl). A three-electrode cell setup was achieved using a titanium sheet as the counter electrode, a Ag|AgCl (3 M KCl_{aq}) as the reference electrode and the fiber electrode as the working electrode, using a Gamry Reference 600 potentiostat/galvanostat (Gamry Instruments). The deposition was carried out under charge control and terminated upon exchanging a total charge of 2.5 µC, that corresponded to a charge density of roughly 125 mC cm^{-2} (tip lateral surface $\approx 2 \times 10^{-5}$ cm^2).

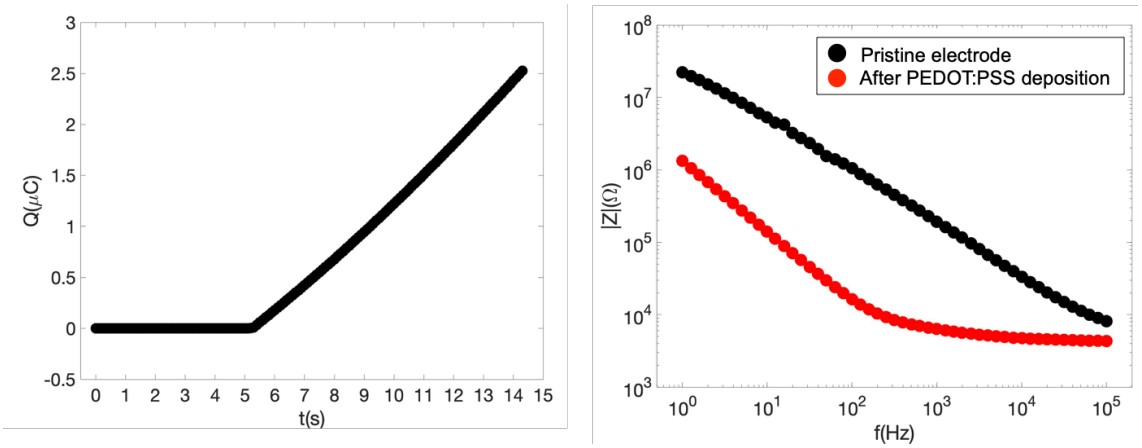

Figure 4.3 a) Chronocoulometric profile of a typical PEDOT/PSS electrodeposition protocol b) Electrochemical Impedance Spectroscopy (EIS) characterization of a pristine Thomas electrode (black scattered slope) and of a PEDOT/PSS-coated one (red scattered slope) in saline solution.

To understand how PEDOT/PSS films grow onto the tip of the electrode, scanning Electronic Microscopy (SEM) was performed (figure 4.4a). The thin PEDOT/PSS film is not uniformly distributed along the whole surface, showing grains at the end of the tip (highlighted by green arrow in Figure 4.4a). Additionally, by means of energy dispersive spectroscopy (EDS) performed in three different regions of the tip (figure 4.4b), it has been possible to observe the anisotropy of the growth of the electrodeposited film. Figure 4.5 shows the three spectra. Characteristics peaks of carbon, sulfur and oxygen confirm the presence of PEDOT/PSS[10]. Spectrum 1 (figure 4.5a), measured to the end of the tip, shows more intense peaks of C, S and O with respect to spectrum 2 (figure 4.5b) and spectrum 3 (figure 4.5c); this testifies how a higher amount of PEDOT/PSS is deposited on the tip while the quantity of the material decreases moving away from the end of the tip. This is clearly related to anisotropies of charge distribution (viz. electrical potential) during chronocoulmetric electrodeposition.

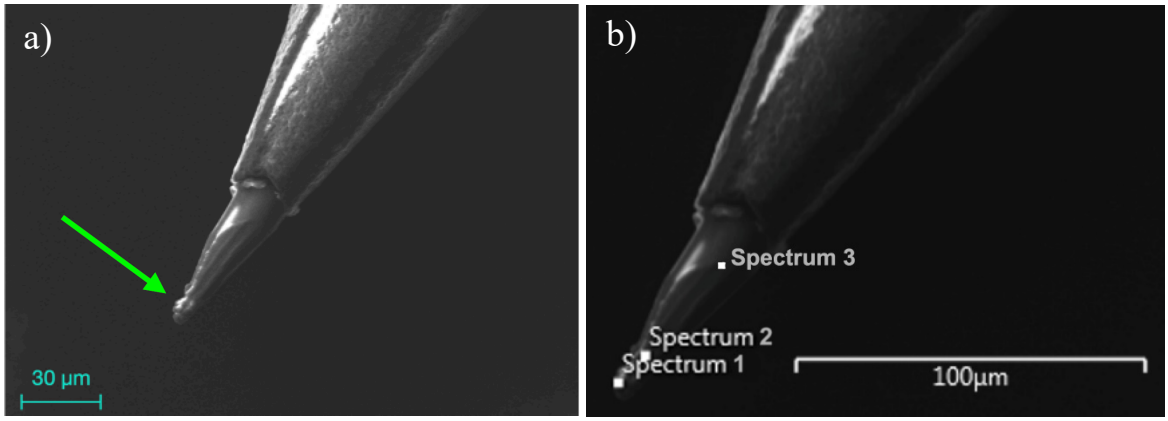

Figure 4.4 a) SEM image of PEDOT/PSS thin films deposited on Thomas electrode tip by electrodeposition, for an overall amount of 5 µC. The image was obtained with a Zeiss EVO 40 SEM. b) The different sites where EDS measurements were conducted. Spectrum 1 was recorded at the end of the tip while the spectrum 2 just above the end of the tip. Spectrum 3 is relative to the farthest region from the tip.

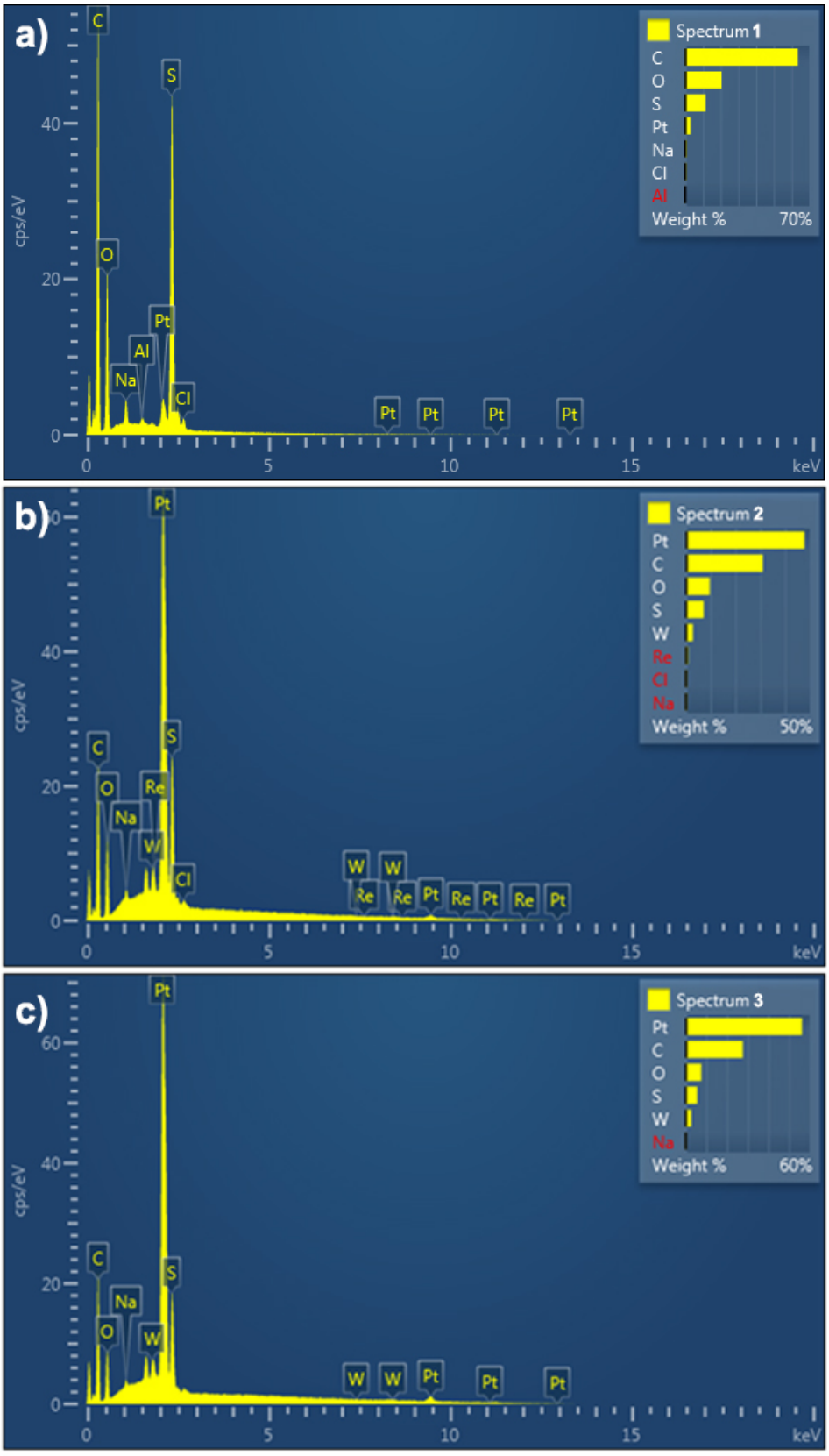

Figure 4.5 EDS analysis of the electrode tip covered by PEDOT/PSS in three different points of its framework. a) EDS spectrum performed on the end of the electrode tip; b) EDS spectrum performed just above the end of the tip; c) EDS spectrum performed on the highest part of the electrode tip.

4.4 Neuromorphic Response Characterization

The proposed synaptic architecture involved two of the above described fiber electrodes, immersed in an electrolyte at a fixed distance of 1 mm; its connection layout is shown in Figure 4.6a. STP was assessed in a 100×10^{-3} M phosphate-buffered saline solution using a two channel Keysight B2912A source-measure unit in a Faraday cage. Low-force terminals of both channels were connected to ground. High-force terminals of channel 1 and channel 2 were connected to the pre-synaptic and post-synaptic electrodes, respectively. Channel 1 was used as a voltage source to pulse the voltage of the pre-synaptic terminal between 0 and −0.5 V, square waves with a 50% duty cycle; channel 2, used as an amperometer, recorded the resulting current at the post-synaptic terminal with a sampling frequency ten times higher than the stimulus frequency, thus keeping constant the number of samples throughout all the experiments (i.e., 10 samples per period). Wave frequency is systematically halved from 2 kHz to 31.25 Hz, resulting in seven investigated frequency values (2 kHz, 1 kHz, 500 Hz, 250 Hz, 125 Hz, 62.5 Hz and 31.25 Hz). Figure 4.6b shows a representative depressive STP current response, elicited at 1 kHz.

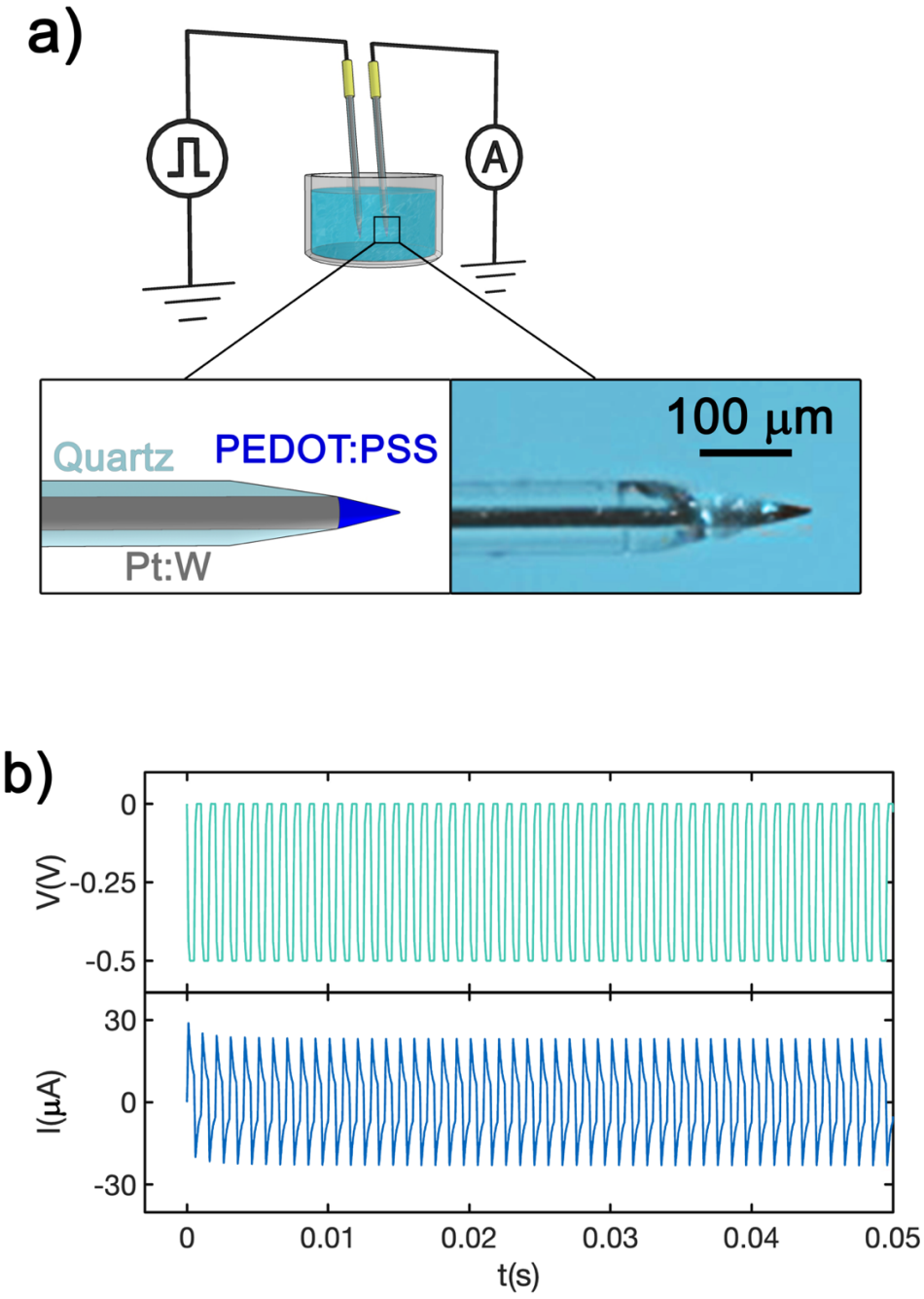

Figure 4.6 a) Schematic representation of the proposed implantable artificial synapse. Inset: schematics and optical micrograph of the tip; b) Example of current depressive response (bottom, dark blue) at the post-synaptic electrode, achieved pulsing the pre-synaptic electrode with a 1 kHz voltage square wave (top, light green).

4.5 Frequency dependent STP response

Figure 4.7 reports a 3D overlay of the STP response at all the investigated frequencies. It is noticeable that: i) at high frequencies the plasticity of artificial synapses exhibits a depressive behavior, ii) a decrease of the input frequency results in the noticeable reduction of the current amplitude coupled to a gradual loss of the depressive behavior; iii) at input frequencies below 250 Hz the STP response turns gradually into a facilitative one. Notice that the facilitative response exhibits always smaller amplitude with respect to the depressive one. It is possible to highlight these effects in Figure 4.8, where current responses to the first ten voltage pulses are reported vs the dimensionless product of time and frequency, $t \cdot f$, and in Figure 4.9, where the envelopes of STP maxima are normalized to the first current spike, $I(0)$ and shown vs the time interval from the stimulation starting time. Figure 4.9 emphasizes the crossover from the depressive to the facilitative behavior of STP from high to low input frequencies.

A physical rationale of this behavior can be formulated by focusing on the mechanistic origin of the depressive STP behavior. At high input frequencies (500 Hz < f < 2 kHz) the current response is dominated by the capacitive displacement current arising in the electrolyte in response to a sudden potential variation at the pre-synaptic electrode. Since the current decays in a time span longer than the inverse of the pulse frequency, the system fails to relax in the time interval between two subsequent spikes and attains a new pseudo-equilibrium determined by the build-up of an effective over-potential at the electrode/electrolyte interface upon continuous stimulation [11].

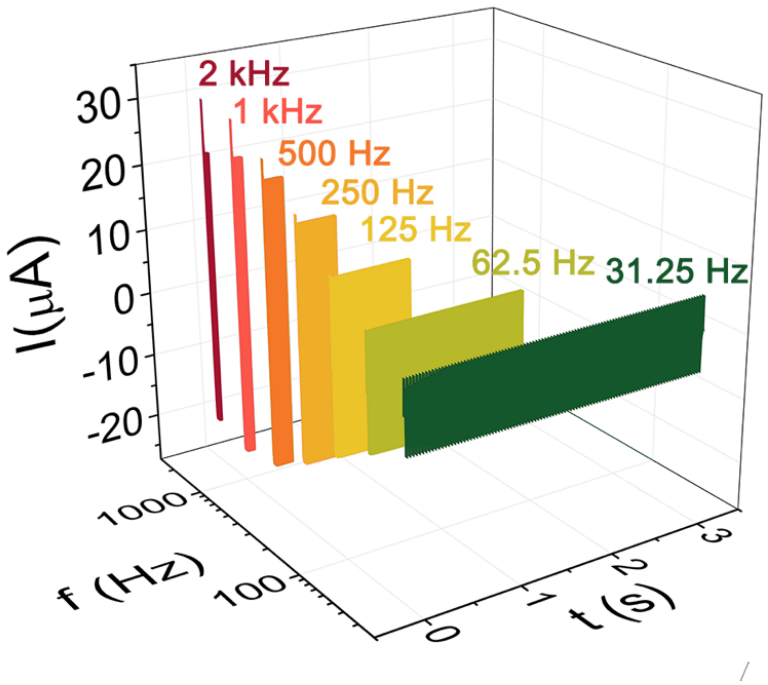

Figure 4.7 Current recorded at the post-synaptic terminal (z-axis) vs stimulation time (x-axis) and input voltage frequency (y-axis)

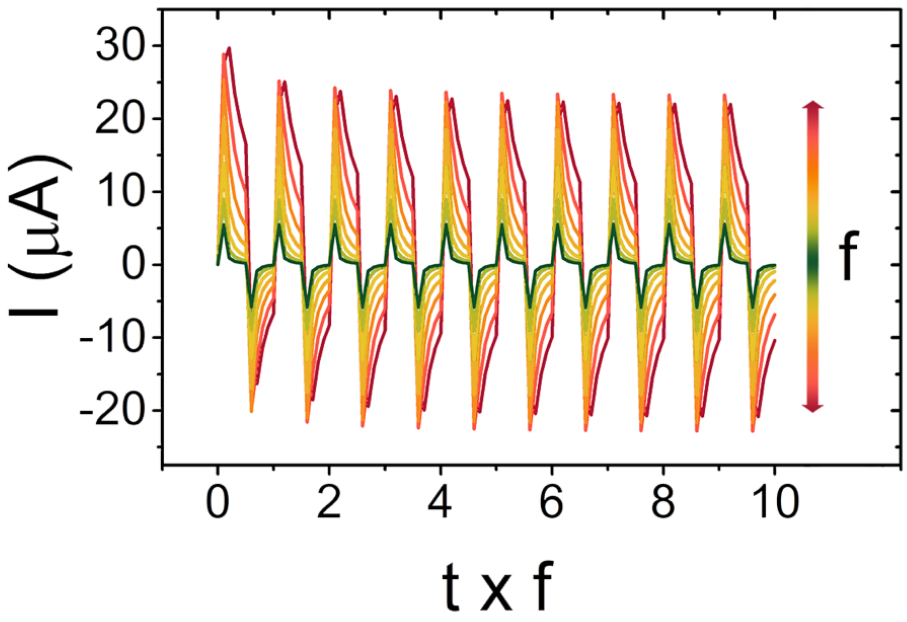

Figure 4.8 Current recorded at the post-synaptic terminal vs the product of time and stimulation frequency (x-axis). The plot emphasizes amplitude decrease and loss of the depressive response as stimulation frequency decreases.

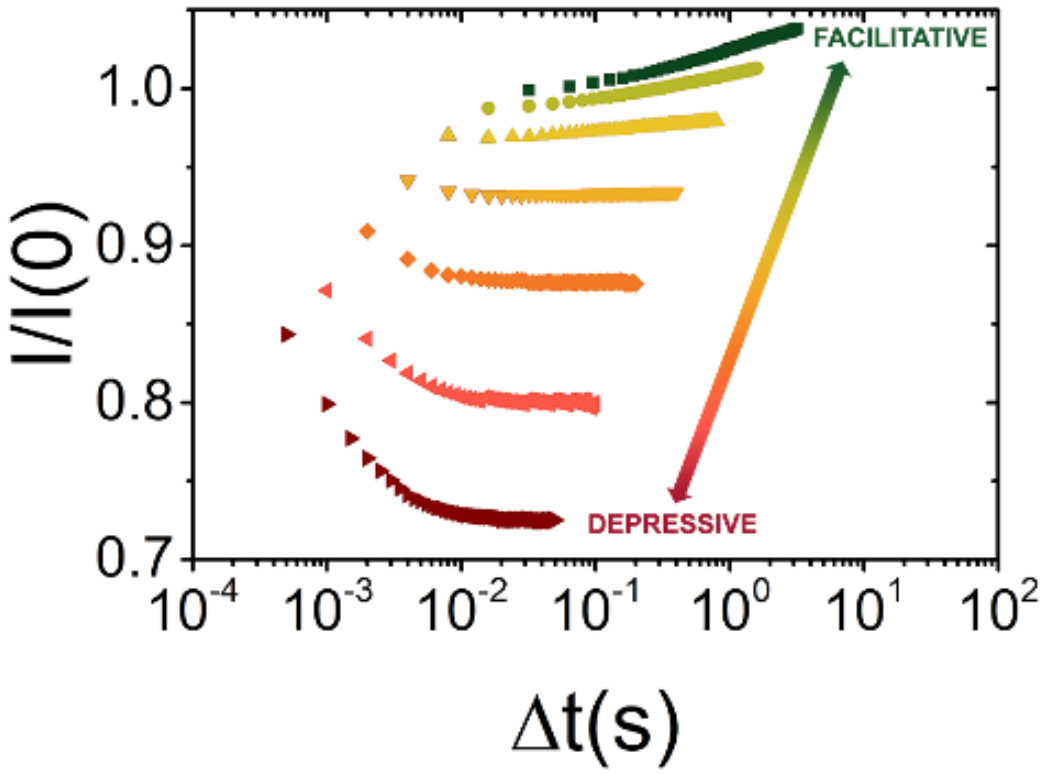

Figure 4.9 Overlay of the normalized current envelopes *I/I(0)* reported vs the time interval spanning from the first maximum to the time value of each maximum, reported in logarithmic scale.

4.6 Equivalent circuit model and mathematical treatment

The Randles equivalent circuit was suitable to describe the depressive STP response[11], but it does not allow one to rationalize the emergency of the facilitative response and its amplitude decrease upon frequency decrease. Indeed, the Randles equivalent circuit exhibits a single frequency-independent RC time constant, which results in a *unique* frequency-independent STP depressive response. It is worth noticing that the rise time of the square pulses (i.e. the derivative of voltage in time) is independent from the chosen stimulation frequency and, accordingly, the displacement current in a Randles circuit would maintain its amplitude at all the input frequencies. In the present artificial synapse, instead, an amplitude decrease is observed in response to pulse frequency decrease.

Both these effects can be accounted for only by introducing a time/frequency-dependent resistive contribution which, in electrochemical systems, is represented by a "pseudo-inductance", as proposed by Gutmann[12]. Such a definition, which identifies the electrochemical pseudo-inductance as a "region of space capable of reversibly storing electric energy kinetically", accounts for the phenomenon at the origin of this varying resistive contribution, namely the motion of ions that drift at the interface between PEDOT/PSS and electrolyte. This motion spans the entire volume of the PEDOT/PSS film and modulates its conductivity. Evidences of such pseudo-inductive behavior in PEDOT/PSS-based systems were reported in studies concerning to non-ideal response of organic electrochemical transistors to both I-V characterization[13] and electrochemical impedance spectroscopy[14]; furthermore, pseudo-inductive behavior is widely explored in the context of energy storage devices[15].

The equivalent circuit used to describe our organic artificial synapse is depicted in Figure 4.10. It involves a minimum modification of the Randles equivalent circuit by adding an inductive term at the PEDOT/PSS||electrolyte interface. In detail, the proposed circuit features a solution resistance (R_E) in series with an RLC section constituted by the double layer resistance (R_{DL}), the double layer capacitance (C_{DL}) and the PEDOT/PSS film pseudo-inductance (L_F). A pulsed voltage source provides square wave stimulation and the amperometer (A) measures the overall output current.

It is possible to provide a quantitative description of the STP response by analytically solving the circuit in Figure 4.10.

The input periodic square wave in the Laplace domain reads:

$$V(s) = \frac{V_0}{s(1+ e^{-s\Theta T})} \tag{4.1}$$

where V_0 is the amplitude, Θ is the duty cycle, T is the period – namely the inverse of the stimulation frequency – and s is the Laplace variable.

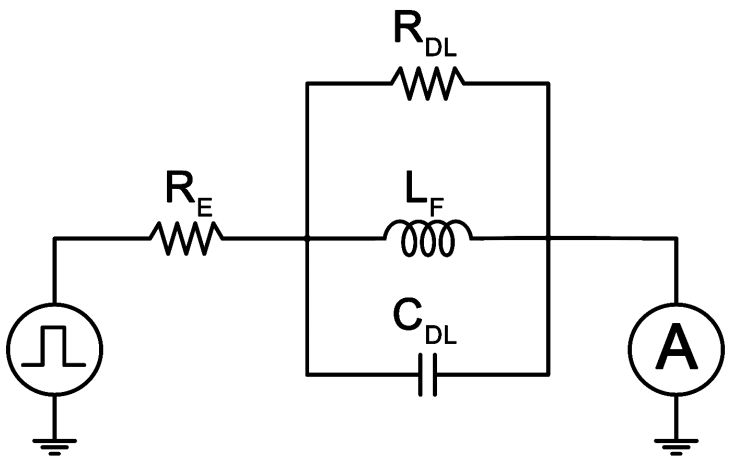

Figure 4.10 Equivalent circuit proposed to model our artificial synapse. It involves an RLC branch composed by the pseudo-inductance of the PEDOT/PSS film *(L_F)* in parallel with the double layer resistance (R_{DL}) and the double layer capacitance (C_{DL}). The RLC branch is in series with the electrolyte resistance (R_E).

In the same domain, the impedances of the passive circuit elements are defined as $Z_{R_E}(s) = R_E$, $Z_{R_{DL}}(s) = R_{DL}$, $Z_{L_F}(s) = sL_F$ and $Z_{C_{DL}}(s) = \frac{1}{sC_{DL}}$. As a consequence, the overall circuit impedance reads as

$$Z(s) = R_E + \left(\frac{1}{R_{DL}} + \frac{1}{sL_F} + sC_{DL}\right)^{-1} \tag{4.2}$$

and, from Ohm's law, one obtains:

$$I(s) = \frac{V(s)}{Z(s)} = \frac{V_0}{s\left(1+e^{-s\Theta T}\right)} \frac{1}{R_E + \left(\frac{1}{R_{DL}} + \frac{1}{sL_F} + sC_{DL}\right)^{-1}} \tag{4.3}$$

Equation (4.3) describes the current in the Laplace domain. Applying the inverse Laplace transform to Equation (4.3), $I(t) = \mathcal{L}^{-1}[I(s)]$, obtaining the current in the time domain, shown in Equation (4.4):

$$I(t) = \frac{V_0}{R_E}\left\{\left[\frac{1-(-1)^{\lfloor -t/\Theta T \rfloor}}{2}\right] + \frac{1}{\rho}\frac{R_{eff}}{R_E}\left[\frac{e^{-Mt}\left(1-\left(-e^{-M\Theta T}\right)^{\lfloor -t/\Theta T \rfloor}\right)}{1+e^{M\Theta T}} - \frac{e^{\Gamma t}\left(1-\left(-e^{\Gamma\Theta T}\right)^{\lfloor -t/\Theta T \rfloor}\right)}{1+e^{-\Gamma\Theta T}}\right]\right\} \tag{4.4}$$

where circuit elements was grouped in the coefficients listed in **Table 1**. $\lfloor x \rfloor$ is the floor function, which returns the greatest integer less than or equal to *x*.

Table 1. Expression of the coefficients in Equation (4.4).

Parameter	Expression	Units
R_{eff}	$\frac{R_{DL}R_E}{R_{DL}+R_E}$	Ω
τ	$C_{DL}R_{eff}$	s
η	$\frac{L_F}{R_{eff}}$	s
ρ	$\sqrt{1-4\frac{\tau}{\eta}} = \sqrt{1-4\frac{C_{DL}R_{eff}^2}{L_f}}$	-
Γ	$\frac{\rho-1}{2\tau}$	Hz
M	$\frac{\rho+1}{2\tau}$	Hz

Equation (4.4) is the analytical expression of the entire STP current profile and can be used to predict the neuromorphic response of an organic artificial synapses, provided that the values of all the equivalent circuit elements are known, else to fit the experimental STP with only four fitting parameters e.g. R_{eff}, R_E, C_{DL}, L_F.

The observed trends can be explained by introducing the time constants τ and η, the former related to the capacitive response and the latter depending on the electrochemical pseudo-inductance. The time constants can be combined in the dimensionless parameter, ρ, which weights the contribution of τ to the two frequency constants, Γ and M, accounting for the facilitative and the depressive response respectively.

The discussion is limited to the domain of real non-negative values for ρ, viz. $0 \leq \rho \leq 1$, and $\frac{\tau}{\eta} = \frac{C_{DL}R_{eff}^2}{L_f} < \frac{1}{4}$. This implies also that $-\frac{1}{2\tau} \leq \Gamma \leq 0$ and $\frac{1}{2\tau} \leq M \leq \frac{1}{\tau}$. In general, Γ is always non-positive, and M is always positive.

Interestingly, $\rho = 1$ yields $\Gamma = 0$ and Equation (4.4) depends only on $M = \frac{1}{\tau}$. This is the case in which L_F approaches infinite and the inductive contribution is negligible, exactly reproducing the behavior of purely depressive STP[11].

The analytical expression for the discrete envelope of STP maxima was then derived, expressing the current as a function of the pulse number (n), instead of time (t). The pulse number, n, is an integer number ranging from 0 to N including the range boundaries, where N is the total number of administered pulses. The number n is obtained by subtracting 1 from the pulse number, *e.g.* for the first spike, $n = 0$.

The time values at which maxima are observed, t_M, can be expressed as a function of the time of the first spike, $t_{M,0}$ and of n, as $t_M(n) = t_{M,0} + nT$. In the proposed experimental conditions, where STP analysis starts one sample before the first voltage pulse, $t_{M,0}$

always corresponds to the sampling time, t_s, which is the inverse of the sampling frequency.

The expression of the maxima time values as a function of *n* can be re-written as:

$$t_M(n) = t_s + nT \tag{4.5}$$

At these time values, the exponential term $\left\lfloor -t/_{\Theta T} \right\rfloor$ from Equation (4.4) can be re-written as:

$$\left\lfloor -\frac{t_M}{\Theta T} \right\rfloor = \left\lfloor -\frac{(t_s+nT)}{\Theta T} \right\rfloor = \left\lfloor -\frac{t_s}{\Theta T} - \frac{n}{\Theta} \right\rfloor . \tag{4.6}$$

In our experiment, where $\Theta = 1/2$, Equation (4.6) reads

$\left\lfloor -\frac{2t_s}{T} - 2n \right\rfloor = \left\lfloor -\frac{2t_s}{T} \right\rfloor - 2n$, as follows from the peculiarities of the floor function, since $2n$ is always integer. In our setup, the sampling time t_s is one tenth of the period T, regardless of the investigated frequency, implying that $\left\lfloor -\frac{2t_s}{T} \right\rfloor = -1$. This can be extended to any STP experiment in which the sampling time is shorter than, or equal to, half of the period *T*: for $0 < t_s \leq \frac{T}{2}$ it will follow that $0 < \frac{2t_s}{T} \leq 1$.

Equation (4.4) is recast in its discrete form:

$$I(n) = \frac{V_0}{R_E}\left\{1 + \frac{1}{\rho}\frac{R_{eff}}{R_E}\left[\frac{e^{-\mathrm{M}t_s}\left(e^{-\mathrm{nMT}} + e^{\mathrm{MT}/2}\right)}{1+e^{\mathrm{MT}/2}} - \frac{e^{\Gamma t_s}\left(e^{\mathrm{n}\Gamma T} + e^{-\Gamma T/2}\right)}{1+e^{-\Gamma T/2}}\right]\right\}. \tag{4.7}$$

because for any *n* value, $(-1)^{-1-2n} = -1$. Equation (4.7) can be further simplified obtaining Equation (4.8), which is the analytical expression of the STP envelope as a function of *n*:

$$I(n) = \frac{V_0}{R_E}\left[\gamma + \alpha e^{-\frac{n}{\theta}} - \beta e^{-\frac{n}{\sigma}}\right], \tag{4.8}$$

where parameters from Equation (4.7) have been grouped as reported in **Table 2**.

Table 2. Parameters in Equation (4.8).

Parameter	Expression
α	$\frac{1}{\rho}\frac{R_{eff}}{R_E}\frac{e^{-\mathrm{M}t_s}}{1+e^{\mathrm{M}T/2}}$
β	$\frac{1}{\rho}\frac{R_{eff}}{R_E}\frac{e^{\Gamma t_s}}{1+e^{-\Gamma T/2}}$
γ	$1+\alpha e^{1/2\theta}-\beta e^{1/2\sigma}$
θ	$\frac{1}{\mathrm{M}T}$
σ	$-\frac{1}{\Gamma T}$

By fitting experimental data at each stimulation frequency, as shown in Figure 4.11a, it is possible to obtain descriptors of the STP behavior from Equation (4.8) where the STP envelope is expressed as the partition of the ohmic current in the electrolyte, V_0/R_E, among a steady state term, whose weight is γ, and two additive depressive and facilitative terms, weighted by the pre-exponential weights α and β, respectively. The latter two decay vs n with decay constants, σ and θ, both positive Thus, when n exceeds either σ and/or θ, the facilitative STP contribution and/or the depressive STP contribution disappear, respectively. Owing to the fact that $|M|>|\Gamma|$, then $\sigma>\theta$ meaning that the depressive STP will be always faster than the facilitative STP, and will disappear within lesser number of pulses.

The overall current response is hence contributed by three terms shown in Equation (4.9):

$$I(n) = I_{SS} + I_D(n) - I_F(n), \tag{4.9}$$

where $I_{SS} = \frac{\gamma V_0}{R_E}$ is the steady-state current, $I_D(n) = \frac{V_0}{R_E}\alpha e^{-\frac{n}{\theta}}$ is a fast-decaying additive contribution to the current which accounts for the depressive STP and $I_F(n) = \frac{V_0}{R_E}\beta e^{-\frac{n}{\sigma}}$ is a slow-decaying subtractive contribution which accounts for the facilitative response. To highlight the role of the weighted current contributions, the depressive, $I_D(n)$, and facilitative, $I_F(n)$, contributions to the STP at 250 Hz response are reported in Figure 4.11b. They both converge to zero plateau value, with different dynamics the slowest, else the one requiring greater number of pulses *n,* being the facilitative one. Figure 4.11c shows the constant steady state current, I_{SS}, and the total current $I(n)$, as obtained from Equation (4.9). As predicted by Equation (4.8), the value of the first maximum, $I(0)= \frac{V_0(\alpha-\beta+\gamma)}{R_E}$ and, since both the exponential terms in Equation (4.8) feature negative exponents, the influence of I_D and I_F in determining the value of $I(n)$ decreases as n increases. The number of pulses which is required for damping each contribution is quantitatively expressed by θ and σ, viz. $n>\theta$ and $n>\sigma$ respectively. This is commented at the end of this section.

By extracting R_E by electrochemical impedance spectroscopy, it is possible to obtain the values of the weights α, β and γ and of the decay constants θ and σ upon fitting of the envelopes. The experimental envelopes were fitted, showing the trends of the parameters vs frequency in Figure 4.11 d-g. This allow to rationalize the observed crossover from facilitative to depressive behavior upon frequency increasing.

The pre-exponential terms, α and β, exhibit opposite trends vs frequency, as shown in Figure 4.11d, with α increasing and β decreasing upon frequency increase. Three frequency ranges are identified amongst which artificial synapses show different STP responses: at low frequencies (<100 Hz), $\alpha \approx 0$, hence $I(n) \approx I_{SS} - I_F(n)$. The net facilitative effect observed results from the exponential decay of $I_F(n)$ for increasing n:

$$I(\infty) = I_{SS} > I(0) \approx I_{SS} - I_F(0). \quad (4.10)$$

This effect is progressively lost upon frequency increase/period decrease since, as discussed above, the pseudo-inductive contribution becomes negligible. Indeed, at higher frequencies (≥500 Hz), $\Gamma = 0$, $\sigma = +\infty$, $L_F \rightarrow +\infty$, $\rho = 1$, leading to $I_F = 0$. Thus, in the absence of inductive contributions, only depressive mono-exponential STP decay can be elicited and Equation (4.8) becomes[11,13,14,16]:

$$I(n) = \frac{V_0}{R_E}\left[1 + \frac{R_{eff}}{R_E}\left[\frac{e^{-Mt_S}}{1+e^{MT/2}}\left(e^{-\frac{n}{\theta}} + e^{\frac{1}{2\theta}}\right) - 1\right]\right]. \quad (4.11)$$

In the intermediate frequency range (from 100 to 500 Hz), around 250 Hz, the facilitative and depressive regimes are co-existing, and a mixed behavior characterized by fast depression and slow facilitation is observed. It must be noticed that the variability range of the depressive weight, α, is one order of magnitude larger than that of the facilitative weight, β; hence, in the facilitative region, the amplitude is more-than-tenfold lower than the amplitude of the depression in the depressive region. This confirms the experimental observation in Figure 4.11a.

The I_D decay constant of the depressive term, θ (Figure 4.11f) accounts for the depressive contribution and increases with the logarithm of the square root of frequency. The I_D decay constant, σ (Figure 4.11g) diverges approaching infinite with a linear dependence on frequency, which accounts for the electrochemical pseudo-inductance representing the kinetic storage of electrostatic energy. This is allowed at low frequency and prohibited at high frequencies. These trends are coherent with the definitions of θ and σ (see Table 2), which depend on M^{-1} and Γ^{-1}, and the period of stimulation T, respectively.

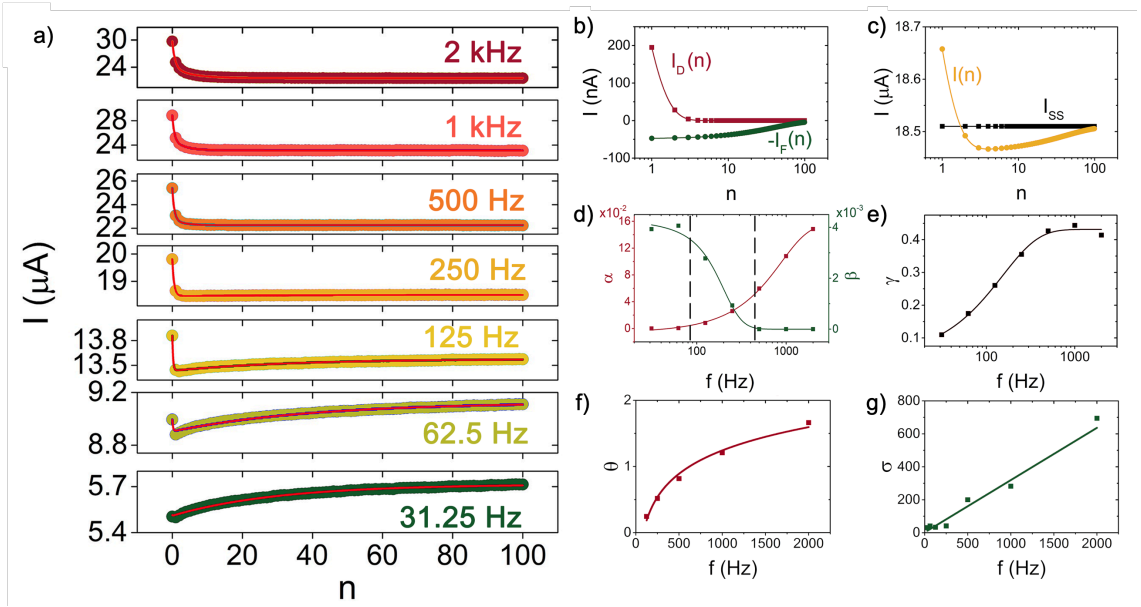

Figure 4.11 a) Envelopes of the maxima of the current response reported vs pulse number at all the investigated frequency values and fitted with Equation (4.9); b) log-lin plot of I_D and $-I_F$ vs pulse number, n, as calculated by fitting STP at 250 Hz with Equation (4.9); c) log-lin plot of constant steady state current, I_{SS}, and full STP envelope, I, vs pulse number, n, as calculated by fitting STP at 250 Hz with Equation (4.9); d) log-lin overlay of the depressive weight, α, and the facilitative weight, β, as a function of frequency. It is possible to distinguish the three frequency regions where the system responds either in a purely depressive manner (high frequencies), in a purely facilitative one (low frequencies) or with a mixed behavior (crossover region); sigmoidal fits are guides for the eye; e) Log-lin plot of the steady state weight, γ, as a function of frequency, showing an high-pass behavior of the electrolyte. The sigmoidal fit is a guide for the eye; f) lin-lin plot of I_D decay constant, θ, as a function of frequency, with logarithmic fit; g) lin-lin plot of I_F decay constant, σ, as a function of frequency, with linear fit.

4.7 Summary of model

In summary, the model predicts the following regimes as a function of the number of pulses supplied, and interestingly, depending on the period T (equivalently on its frequency 1/T), or, more precisely, the ratio T/τ:

1. *$n>>\sigma>\theta$ plateau;*
2. *$n<\sigma$ and $n>>\theta$ facilitative STP, not depressive STP;*
3. *$n<\theta<\sigma$ facilitative STP and depressive STP coexist. The weights α and β determine which STP behavior dominates. Since $\alpha>>\beta$ at high frequencies, hence depressive STP dominates; viceversa $\alpha<\beta$ at low frequencies makes facilitative STP to dominate.*
4. *$n<\theta<<\sigma$ depressive STP, not facilitative STP. This implies that $MT>>-\Gamma T$, and hence $\rho T/\tau>>0$. The maximum depressive STP is observed for $\rho=1$ and $T>>\tau$. This is the situation where, de facto, one applies single pulses, largely spaced, so the system does not retain memory of the previous ones. On this particular case, somewhat counterintuitively, the very slow input wave yields a depressive STP.*

From the operation point of view, especially to obtain devices with targeted response, this model appears useful for estimating how many pulses are actually needed for inducing a depressive STP and/or facilitative STP.

4.8 Artificial synapses for dopamine sensing

4.8.1 Background on dopamine sensing

Dopamine (DA) is one of the neurotransmitters mainly involved in human behavior and physical processes concerning motivation and though[17]. The time monitoring of dopamine level is necessary to control its healthy concentration which is significant for the onset of neurodegenerative diseases like Parkinson Disease. DA physiological concentration lies in the nanomolar range[18] making it more complex to be detected.

Nowadays, approaches to dopamine sensing are based on electrochemical techniques[19], in particular amperometry[20,21] and cyclic voltammetry. In such experiments, DA in solution is oxidized to o-quinone and the recorded current is proportional to DA concentration. Indeed, in cyclic voltammetry (CV), the voltage at which the center of the oxidative (cathodic) peak is observed is peculiar of the redox exchanger dissolved in solution. More importantly, peak intensity is related to concentration of the electroactive molecule itself[22]. In real systems, DA can be found diluted in a complex solution called cerebrospinal fluid (CSF) which is a mixture of ions and molecules, including DA catabolites. Therefore, *in vivo* dopamine sensing requires the tailoring of a system which enables to specifically discriminate DA from such other moieties, which could act as interfering agents. In this scenario, voltammetric methods are among the most suitable techniques[23–26]. Despite the tremendous advances in such measurement strategies, which led to the capability of exactly quantifying DA in the striatum, they suffer from the presence in the CSF of interfering species with oxidation potentials similar to that of DA, like ascorbic acid (AA) and Uric acid (UA). Furthermore, DA oxidation can produce melanin polymeric films, which affect the device sensibility. Another approach to DA

sensing is offered by Electrolyte Gated Organic Transistors (EGOTs), where the sensing mechanism is due the capacitive coupling with the (semi)conductive channel without involving faradic processes. EGOTs have been in facts demonstrated as label-free dopamine biosensors[27,28] down to a concentration of 1 pM in model aqueous solutions.

As aforementioned (see chapter 1), organic neuromorphic architectures open unprecedented possibilities towards dopamine detection, since they do not make advantage of voltammetric parameters and use - as main observable related to DA concentration - the STP time constant, albeit in model solutions.

Aim of the present study is to extend the applicability scenario of such approaches to complex systems, starting from an *in vitro* calibration in artificial Cerebrospinal Fluid (aCSF[29]) (10 nM < [DA] < 200 nM, in the range of interest for Parkinson's disease) followed by *in vivo* validation. It is discussed here how the peculiar technological needs of an *in vivo* DA assessment demand layout modifications, which do not modify the sensing principle, switching from the device discussed in section 4.1 to a simplified architecture which, by making advantage of the grounding of the animal, enables mono-electrode systems. This modified architecture is necessary for devising precise localization strategies for the electrode and, subsequently, an unambiguous mapping of DA local concentration in the brain.

4.8.2 *In vitro* Dopamine sensing

The sensor response to the increasing concentration of DA must be calibrated through an *in vitro* DA dose curve, using a layout which is as close as possible to the finally implanted one. For this reason, the *in vitro* set up needs to be modified from the original

two electrode artificial synapse to a Mono-Electrode Neuromorphic Unit, here termed MENU.

In the 4.4 and 4.5 sections the frequencies were systematically investigated from 2 kHz to 31,25 Hz halving the period. It was observed that the right balance in terms of pseudoinductive and capacitive contributions to STP is achieved for 125 Hz frequency. As a consequence, 125 Hz was chosen as operational frequency for the MENU.

Dopamine (DA) is dosed using a preeflow eco-pen 300 device connected to an eco-CONTROL EC200-K flow control system. DA is released in 10 seconds increments at a flow rate set at 50 nL/s from a DA stock solution. The evolution of DA concentration for each step can be calculated from the equation (4.12):

$$[DA](t) = \frac{[DA]_0 \phi t}{V_i + \phi t} \tag{4.12}$$

Where $[DA]_0$ is the concentration of the dopamine stock solution (1 mM in aCSF - pH 7,4 stabilized with H_3PO_4 50 mM), ϕ is the flux (L/s), t is the time (s) and V_i is the initial volume (50 mL) of aCSF. For each concentration, ten STP trains are administered and their maxima are fitted by the equation 4.13, obtained from equation 4.8, by posing $\gamma' = \frac{V_0}{R_E}\gamma$; $\alpha' = \frac{V_0}{R_E}\alpha$; $\beta' = \frac{V_0}{R_E}\beta$, the equation 4.8 becomes:

$$I(n) = \gamma' + \alpha' e^{-\frac{n}{\theta}} - \beta' e^{-\frac{n}{\sigma}} \tag{4.13}$$

The obtained fitting parameters are averaged among the ten repeated measurements. In figure 4.12, the MENU architecture coupled with the with micro-dosing system set up is schematically reported.

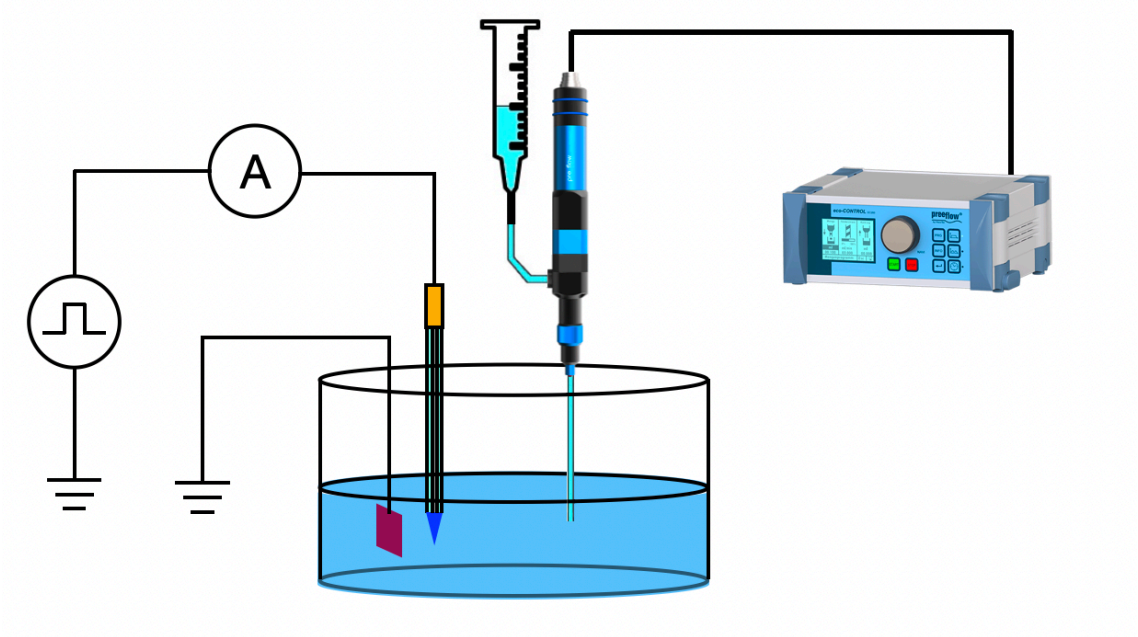

Figure 4.12 MENU instrumental set up for *in vitro* measurements. It is composed by a Thomas electrode with the tip covered by PEDOT/PSS (blue tip) and a platinum plate as ground. In the becher, containing aCSF, is fluxed DA every 10 seconds with eco-CONTROL EC200-K flow control system, gradually increasing its concentration from 10 nM to 200 nM.

The flux of dopamine leads to a visible variation in the STP envelope profile visible in figure 4.13.

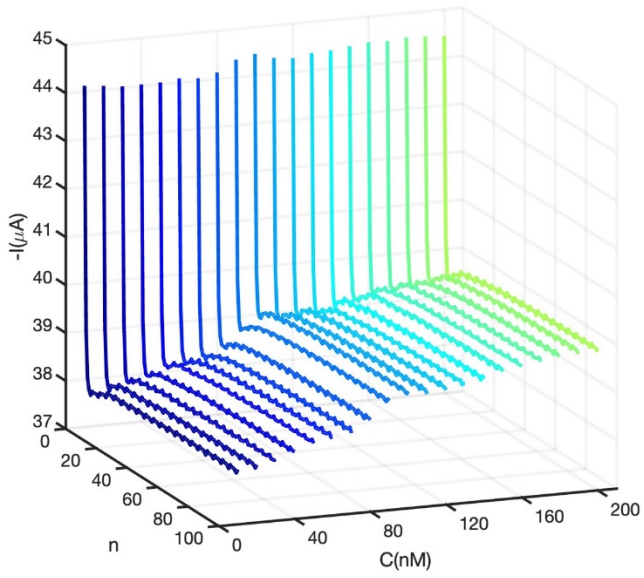

Figure 4.13 DA dose curve. The 3D-plot shows the current profile at each DA concentration in the range of 10 nM to 200 nM. Along the z-axis is showed the current recorded to the synaptic electrode versus the DA concentration (x-axis) and number of pulses (y-axis).

Amongst the multiple parameters derived by STP maxima fitting, the one that exhibits a marked correlation with DA concentration is θ, whose normalized percentage variation with respect to lowest examined dopamine concentration is reported vs [DA] in Figure 4.14. S_θ can be calculated starting from θ values, obtained by fitting the STP envelope at each DA concentration, according to equation 4.14.

$$S_\theta(\%) = \left|\frac{\theta - \theta_0}{\theta_0}\right| \times 100 \tag{4.14}$$

This signal variation is due the increase of the polymeric film capacitance upon the strong interaction between dopamine and PEDOT/PSS[11]. As a consequence of this promising result, an *in vivo* experiment has been performed.

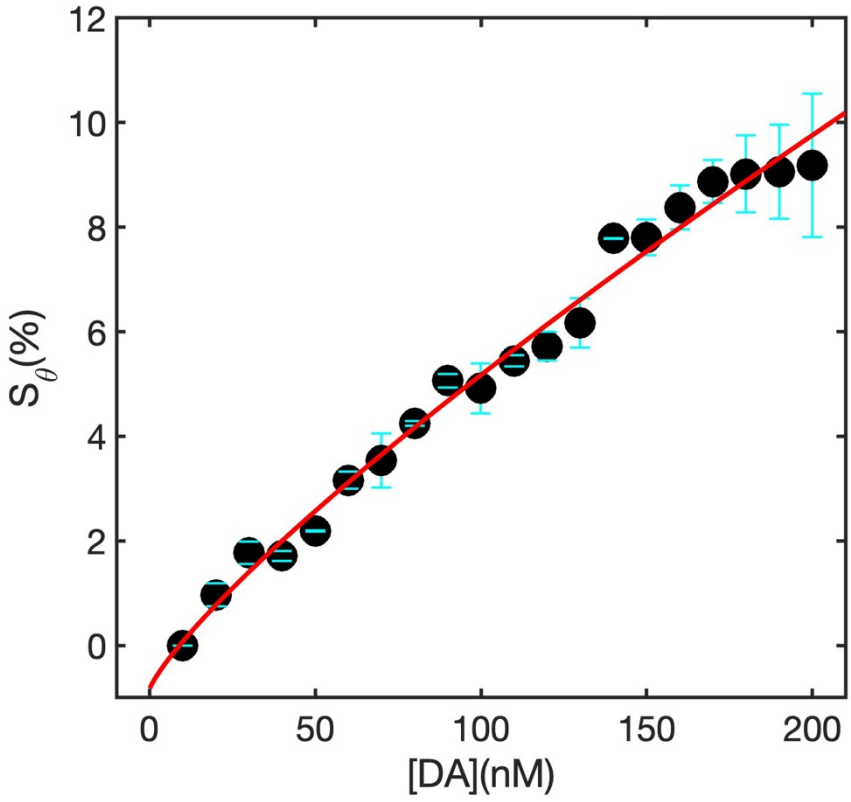

Figure 4.14 Percent of signal (S_θ) variation vs DA concentration in the range of 10 nM to 200 nM. The error bars are referred to the SEM between 2 measurements. The red slope (power fit) is a guide for eyes.

4.8.3 *In vivo* dopamine sensing

One adult male Wistar rat, weighing 300 g, was used for the *in vivo* session. The experimental protocol was designed in compliance with Italian law regarding the care and use of experimental animals (DL26/2014), and approved by the institutional review board of the University of Ferrara and the Italian Ministry of Health (permission n. 989/2020-PR). Adequate measures were taken to minimize animal pain as well as the number of animals used, according to the three Rs principle[30]. Rat was initially anaesthetised with ketamine hydrochloride (80 mg/Kg), and supplementary ketamine injections (4 mg/Kg, given as required, typically every 25–30 min) were used for the duration of the session to maintain long-latency and sluggish hindlimb withdrawal upon pinching the hindfoot[31,32] (stage III-1 and III-2).

The ketamine-anaesthetised rat was placed in a stereotaxic apparatus and a craniotomy was performed to expose the cerebral cortex (Fig. 4.15).

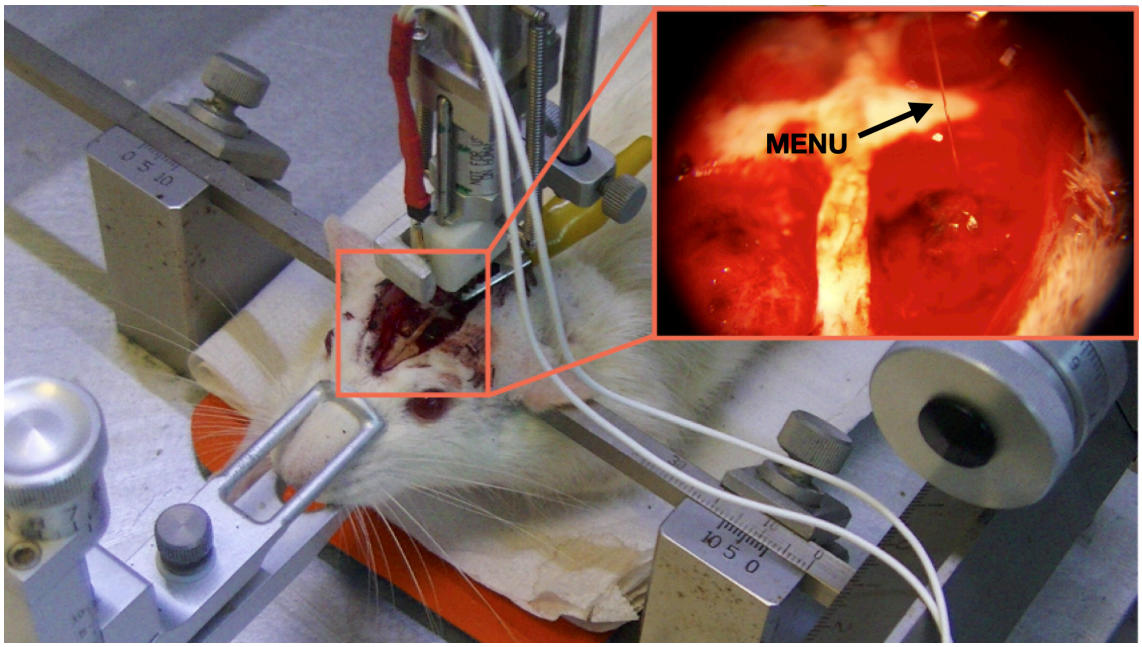

Figure 4.15 Rat craniotomy performed by placing the rat on the stereotaxic apparatus. In the inset is reported the implanted MENU into the striatum taken with optical micrograph.

The dura remained intact, and was kept moist with saline. The electrode was lowered (Fig. 4.15 inset) perpendicularly according to the following coordinates[33] from bregma: AP= +1.2 mm, ML= +2.5 mm (figure 4.16 A). STP stimulation was delivered at six depth values, with 1 mm-steps (figure 4.16 B), using the MENU mounted on a microadvancer (Kopf Micropositioner 2650, David Kopf Instruments, Tujunga, CA, USA), using as ground a caudally implanted screw. At the end of the experimental session, the animal was deeply anaesthetised with Zoletil 100 (10 mg/Kg; Virbac Laboratories, Carros, France) and sacrificed.

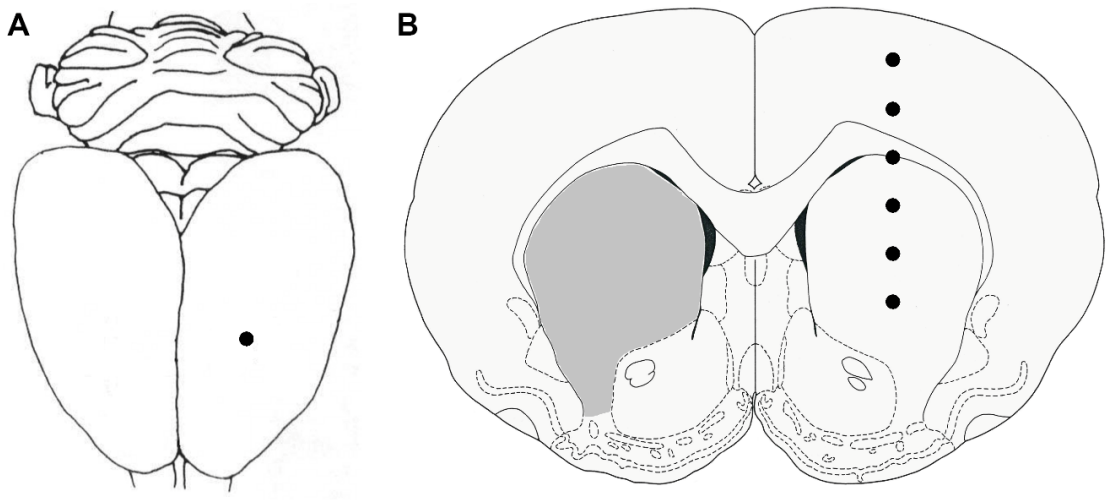

Figure 4.16 Dopamine detection in rat brain. **A,** Top view of the rat brain, showing MENU penetration site (dark circle; AP=1.2 and ML=2.5 from bregma). **B,** Coronal section of the rat brain (AP=1.2 from bregma), showing the six different depths (1 mm-step from dura) for the dopamine detection (dark sites). Striatum was highlighted in grey at the contralateral hemisphere.

The final experiment in this work of thesis concerns the employment of the MENU to *in vivo* dopamine sensing. The detection, made at six different brain- depths, starts from the dura madre (poor in dopamine) and goes deep to the inner part of striatum (rich in dopamine). For each depth the same STP protocol used for the *in vitro* experiment was applied, as described in section 4.2.3. Figure 4.17 reports the depressive pulse constant,

θ, in function of brain-depth (*d(mm)*). Here it is possible to clearly observe two different zones; the first, for *d* values ranging from 1mm to 3 mm, shows constant θ value due non-significant variation of DA concentration. It is worth noticing how, while moving from d= 3 mm to d=4 mm (i.e. entering the striatum), an abrupt increase of θ is observed. It is possible to hypothesize that, in the presence of such high levels of dopamine, the MENU rapidly saturates to a plateau for d > 5mm, as suggested by its trend in Figure 4.14.

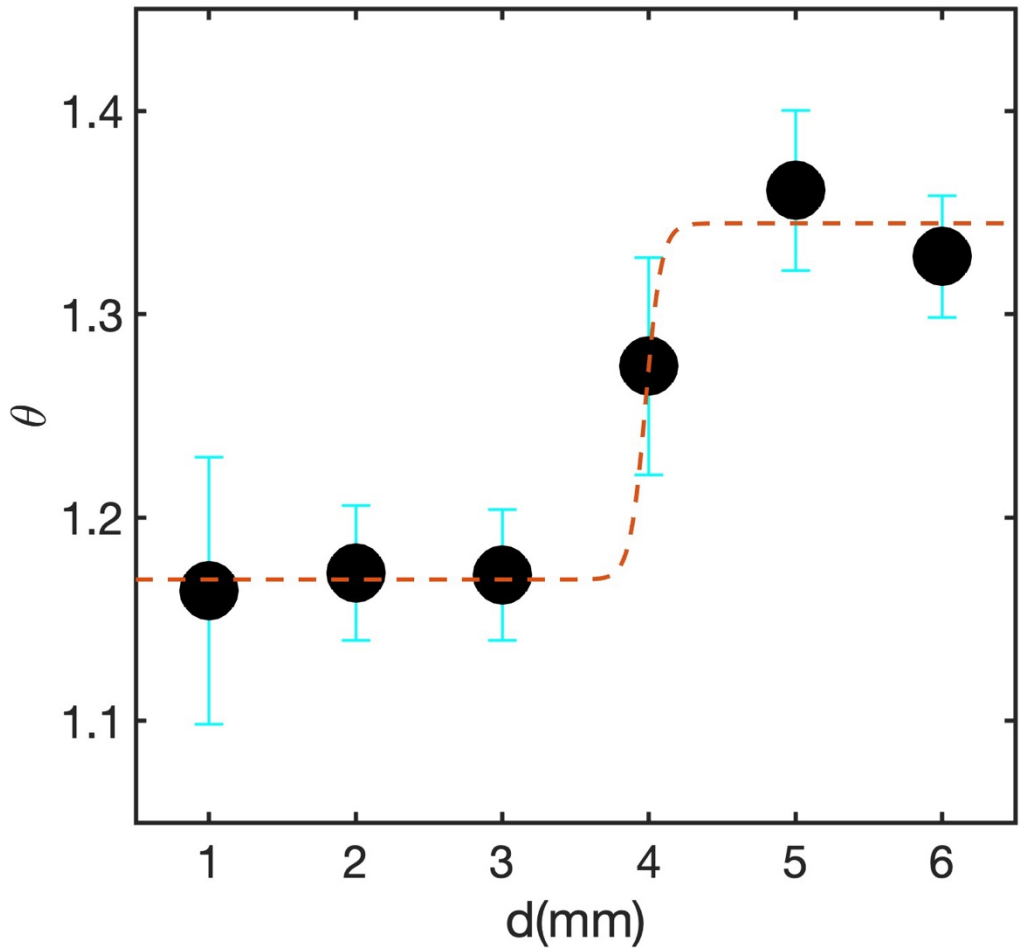

Figure 4.17 Depressive pulse constant, θ, vs brain-depth, d(mm). The red dashed slope, Boltzmann fit equation, is reported as guide for eyes. The error bars represent the standard deviation among ten repeated measurements at each depth.

References

1. Reitboeck, H. J. Fiber microelectrodes for electrophysiological recordings. *J. Neurosci. Methods* **8**, 249–262 (1983).
2. De Faveri, S. *et al.* Bio-inspired hybrid microelectrodes: A hybrid solution to improve long-term performance of chronic intracortical implants. *Front. Neuroeng.* **7**, 1–12 (2014).
3. Richardson-Burns, S. M., Hendricks, J. L. & Martin, D. C. Electrochemical polymerization of conducting polymers in living neural tissue. *J. Neural Eng.* **4**, (2007).
4. Kim, D. H., Wiler, J. A., Anderson, D. J., Kipke, D. R. & Martin, D. C. Conducting polymers on hydrogel-coated neural electrode provide sensitive neural recordings in auditory cortex. *Acta Biomater.* **6**, 57–62 (2010).
5. Ansaldo, A., Castagnola, E., Maggiolini, E., Fadiga, L. & Ricci, D. Superior electrochemical performance of carbon nanotubes directly grown on sharp microelectrodes. *ACS Nano* **5**, 2206–2214 (2011).
6. Baranauskas, G. *et al.* Carbon nanotube composite coating of neural microelectrodes preferentially improves the multiunit signal-to-noise ratio. *J. Neural Eng.* **8**, 66013 (2011).
7. Carli, S. *et al.* Electrodeposited PEDOT:Nafion Composite for Neural Recording and Stimulation. *Adv. Healthc. Mater.* **8**, 1–10 (2019).
8. Vomero, M. *et al.* Highly Stable Glassy Carbon Interfaces for Long-Term Neural Stimulation and Low-Noise Recording of Brain Activity. *Sci. Rep.* **7**, 40332 (2017).
9. Boehler, C., Oberueber, F., Schlabach, S., Stieglitz, T. & Asplund, M. Long-Term Stable Adhesion for Conducting Polymers in Biomedical Applications: IrOx and

Nanostructured Platinum Solve the Chronic Challenge. *ACS Appl. Mater. Interfaces* **9**, 189–197 (2017).

10. Khan, M. U., Hassan, G., Raza, M. A., Bae, J. & Kobayashi, N. P. Schottky diode based resistive switching device based on ZnO/PEDOT:PSS heterojunction to reduce sneak current problem. *J. Mater. Sci. Mater. Electron.* **30**, 4607–4617 (2019).
11. Giordani, M. *et al.* Neuromorphic Organic Devices that Specifically Discriminate Dopamine from Its Metabolites by Nonspecific Interactions. *Adv. Funct. Mater.* **30**, 1–13 (2020).
12. Gutmann, F. Electrochemical Pseudo-Inductances. *J. Electrochem. Soc.* **112**, 94 (1965).
13. Tu, D. & Forchheimer, R. Self-oscillation in electrochemical transistors: An RLC modeling approach. *Solid. State. Electron.* **69**, 7–10 (2012).
14. Pecqueur, S., Lončarić, I., Zlatić, V., Vuillaume, D. & Crljen, Ž. The non-ideal organic electrochemical transistors impedance. *Org. Electron.* **71**, 14–23 (2019).
15. Breitkopf, C. & Swider-Lyons, K. *Springer Handbook of Electrochemical Energy*. (Springer, 2016).
16. Hu, Y. *et al.* Diverse Synaptic Plasticity Induced by the Interplay of Ionic Polarization and Doping at Salt-Doped Electrolyte/Semiconducting Polymer Interface. *ACS Omega* **2**, 746–754 (2017).
17. Ethan S. Bromberg-Martin, M. M. and O. H. Dopamine in motivational control: rewarding, aversive, and alerting. *Neuron* **68**, 815–834 (2010).
18. Oertel, W. & Schulz, J. B. Current and experimental treatments of Parkinson disease: A guide for neuroscientists. *J. Neurochem.* 325–337 (2016) doi:10.1111/jnc.13750.

19. Lakard, S., Pavel, I. A. & Lakard, B. Electrochemical biosensing of dopamine neurotransmitter: A review. *Biosensors* **11**, (2021).

20. Lupu, S. *et al.* Development of amperometric biosensors based on nanostructured tyrosinase-conducting polymer composite electrodes. *Sensors (Switzerland)* **13**, 6759–6774 (2013).

21. Njagi, J., Chernov, M. M., Leiter, J. C. & Andreescu, S. Amperometric detection of dopamine in vivo with an enzyme based carbon fiber microbiosensor. *Anal. Chem.* **82**, 989–996 (2010).

22. Robinson, D. L., Hermans, A., Seipel, A. T. & Wightman, R. M. Monitoring rapid chemical communication in the brain. *Chem. Rev.* **108**, 2554–2584 (2008).

23. Castagnola, E. *et al.* In Vivo Dopamine Detection and Single Unit Recordings Using Intracortical Glassy Carbon Microelectrode Arrays. *MRS Adv.* **3**, 1629–1634 (2018).

24. Taylor, I. M., Patel, N. A., Freedman, N. C., Castagnola, E. & Cui, X. T. Direct in Vivo Electrochemical Detection of Resting Dopamine Using Poly(3,4-ethylenedioxythiophene)/Carbon Nanotube Functionalized Microelectrodes. *Anal. Chem.* **91**, 12917–12927 (2019).

25. Castagnola, E. *et al.* Glassy carbon microelectrode arrays enable voltage-peak separated simultaneous detection of dopamine and serotonin using fast scan cyclic voltammetry. *Analyst* **146**, 3955–3970 (2021).

26. Castagnola, E., Garg, R., Rastogi, S. K., Cohen-Karni, T. & Cui, X. T. 3D fuzzy graphene microelectrode array for dopamine sensing at sub-cellular spatial resolution. *Biosens. Bioelectron.* **191**, 113440 (2021).

27. Casalini, S., Leonardi, F., Cramer, T. & Biscarini, F. Organic field-effect transistor for label-free dopamine sensing. *Org. Electron.* **14**, 156–163 (2013).

28. Gualandi, I. *et al.* Selective detection of dopamine with an all PEDOT:PSS Organic Electrochemical Transistor. *Sci. Rep.* **6**, 1–10 (2016).

29. abcam. https://www.abcam.com/protocols/brain-slice-electrophysiology-video-protocol. (2017).

30. Russell, W. M. . & Burch, R. . Principle of Human Experimental Techniques. 1–229 (1959).

31. Friedberg, M. H., Lee, S. M. & Ebner, F. F. Modulation of receptive field properties of thalamic somatosensory neurons by the depth of anesthesia. *J. Neurophysiol.* **81**, 2243–2252 (1999).

32. Tandon, S., Kambi, N. & Jain, N. Overlapping representations of the neck and whiskers in the rat motor cortex revealed by mapping at different anaesthetic depths. *Eur. J. Neurosci.* **27**, 228–237 (2008).

33. Herman, J. P. & Watson, S. J. *The rat brain in stereotaxic coordinates (2nd edn)*. *Trends in Neurosciences* vol. 10 (1987).

5. Conclusions

In conclusion, in this work of thesis is centered on the development and investigation of novel neuromorphic architectures. The first one is based on electrolyte-gated organic transistors (working either in depletion or in accumulation) developed and validated, allowing reversible tuning of amplitude, rate and current plateau of the neuromorphic depressive response upon V_{GS} modulation. By properly controlling V_{GS}, it is possible to shift the baseline current, the amplitude and the steepness of neuromorphic behavior in the channel of organic electronic EGOT-based neuromorphic devices, preluding to multilevel memory writing and frequency dependent controllable decisional nodes in more complex neuromorphic organic circuitry, as well as tailorable sensitivity in STP-based sensors.

The second architecture, made the implantable organic artificial synapse built on intracortical microelectrode whose tip are coated with electrodeposited PEDOT/PSS films, represent the main result of this work. Optimization of this architecture involved a systematic investigation of the STP behavior in response to variations of the pre-synaptic frequency over two decades and enabled modeling of the observed transition from facilitative to depressive behavior upon frequency increase. In particular, it has been possible to explain this transition and the coexistence of both depressive and facilitative behaviors in one single neuromorphic device by introducing a frequency-dependent inductive contribution in parallel to the most accepted equivalent circuit model for depressive STP. Laplace analysis of the equivalent circuit allowed us to reproduce the STP current trends vs time and to discretize the envelope of the current maxima vs the number of input voltage pulses, thus providing a set of quantitative descriptors of neuromorphic response of such devices.

We here highlight the novel and important results for organic neuromorphic devices: i) at a given frequency, STP manifests itself either as depressive or facilitative, else as a

coexistence of the two regimes; ii) the input frequency determines what of the three regimes is the dominant one; thus, in principle, even a "pure" frequency input to an organic neuromorphic device that was not conditioned before (then, does not retain memory of its previous history), allows one to instruct the system to respond in one of the three modes; iii) the coexistence of the depressive and facilitative regimes, the former with faster and the second with slower timescales, is, in reality, the "unifying" or "universal" regime. The number of input voltage pulses determines whether we observe only depressive (one needs many more pulses for the system to turn into facilitative STP at high frequencies), facilitative (depressive is only for a few pulses at the onset of stimulation at low frequencies), or both. The number of pulses is, therefore, an independent control of the STP response that the system outputs, iv) the amplitude of STP is another valuable information about the input signal, as we noticed that high frequency tends to maintain the amplitude of the response, whereas at low frequencies we observe a net lowering of the amplitude. It turns out that information flow is coded not only in the timescales but also on the STP amplitudes.

Another relevant result is that we have been able to link the timescales and their interplay to the presence of a simple, albeit new, element in the equivalent circuit, viz. the electrochemical pseudo-inductance, that accounts to some extent on the ion gradient created inside the active material (PEDOT/PSS in our case) and that progressively builds up an internal potential against ion diffusion across the volume, as confirmed by the scaling of pseudo-inductive behavior in organic electronic devices with electrolyte ion concentration[1] and by other evidence that we reported recently, namely the saturation of effective capacitance and electroactive area vs the volume of the active layer[2]. The novelty of these aspects should stimulate research towards ways of controlling, or finely tuning, the inductance element in the framework of RLC circuits. This is an intriguing

finding, since most of the previous reports addressed depressive STP and related its timescale to an RC equivalent circuit. It was also observed the emergence of facilitative response when higher frequency stimulation (driving the system into depressive STP) is followed by a low frequency stimulation. However, this is the first time to our knowledge, where the crossover between the two regimes is clearly demonstrated to occur also within a constant frequency stimulation, and how this coincides with the inductive element taking a finite value.

Finally, the importance of this work from an electrophysiology point of view is that it demonstrates the fabrication and proof-of-concept operation of implantable artificial synapses. As simple as the architecture may appear, it is a change of paradigm in electrophysiology as it would become possible to design components and circuitry with targeted response to specific physiologically relevant frequency patterns.

This is an attractive feature, as it will move the frontiers of (passive) electrophysiological recording to devices able to recognize specific signals related to a given pathology or to transient deficits. These characteristics, together with the advantages of organic neuromorphic devices in terms of biocompatibility and power consumption, are worth to be explored, in view of developing standalone therapeutic devices, able to monitor electrical and/or chemical signals, and react accordingly when the monitored features match those of the target signal, for instance by controlling local drug delivery or administering a voltage stimulus in closed loop architectures.

Within this context we demonstrated that the methodological and analytical tools herein proposed widen the applicability range of organic artificial synapses, enabling tunable STP for sensing and signal processing for in *in vivo* applications. Indeed, the translational potential of implantable artificial synapses has been extensively investigated towards the assessment of dopamine detection and quantification in systems of growing complexity,

starting from aCSF and moving towards *in vivo* scenario. This demanded the design of a simplified artificial synapse architecture to translation: the Mono-Electrode Neuromorphic Unit - MENU.

Conversely to its predecessors, two terminal devices operated in simple model solutions[3], MENU architecture retains dopamine sensitivity also in the presence of the variegated electrolytic environment of aCSF (i.e. in the presence of both monovalent and divalent cations strongly interacting with PSS^-). This promising results, coupled to the *ad hoc* integration of the MENU concept on intracortical devices, led to *in vivo* mapping of dopamine presence. The versatility, sensitivity and processability makes MENU a good candidate tool to be integrated in the next generation implantable loco-regional therapy architectures for neurological disorders; especially for Parkinson's disease, to monitor in real time the course of the pathology by detecting the presence of dopamine in a peculiar site and/or dopamine concentration fluctuations in the brain.

References

1. Pecqueur, S., Lončarić, I., Zlatić, V., Vuillaume, D. & Crljen, Ž. The non-ideal organic electrochemical transistors impedance. *Org. Electron.* **71**, 14–23 (2019).
2. Bianchi, M. *et al.* Scaling of capacitance of PEDOT:PSS: Volume: Vs. area. *J. Mater. Chem. C* **8**, 11252–11262 (2020).

List of figures

List of attended conferences and workshop

1st Workshop on Organic Neuromorphic Devices, Ferrara, IT [2019]

OrBItaly (Organic BIoelectronics Italy), Napoli [2019]

1st School of Organic Bioelectronics, Napoli [2019]

List of publications

Tunable Short-Term Plasticity Response in Three-Terminal Organic Neuromorphic Devices. Michele Di Lauro, Anna De Salvo, **Gioacchino Calandra Sebastianella**, Michele Bianchi, Stefano Carli, Mauro Murgia, Luciano Fadiga, and Fabio Biscarini. *ACS Appl. Electron. Mater.* 06 Jul 2020.

Implantable Organic Artificial Synapses Exhibiting Crossover between Depressive and Facilitative Plasticity Response. **Gioacchino Calandra Sebastianella**, Michele Di Lauro, Mauro Murgia, Michele Bianchi, Stefano Carli, Michele Zoli, Luciano Fadiga, Fabio Biscarini. *Adv. Electron. Mater.* 2021, 7, 2100755.

Ringraziamenti

Il dottorato è stato finora la parte della mia vita più intensa, combattuta e che soprattutto ha tirato fuori ed intensificato alcuni tratti del mio carattere. Ho pensato molte volte di lasciare ed ogni volta fare esattamente l'opposto era un punto di forza che aggiungevo alla mia crescita personale. Le figure importanti di questi anni sono state diverse:

- In primis il professore Fabio Biscarini, scienziato e uomo di grande carisma e competenza che ha fatto si che io potessi mettermi in gioco.
- Il professore Michele Zoli per essere stato sempre presente e propositivo in ogni fase del mio percorso.
- Il professore Luciano Fadiga per avermi concesso di frequentare i laboratori IIT sotto la sua supervisione.
- La mia famiglia che mi è stata sempre vicino nei momenti più difficili ed importanti della mia vita.
- A tutti i miei colleghi ed amici per esserci ed esserci stati.
- Un particolare e commosso ringraziamento va al Dottor Michele Di Lauro il quale mi ha insegnato tutto quello che so sia come scienziato che parzialmente come uomo. Il suo insegnamento principale è stato: "Concentrati sulle possibilità di successo e non su quelle di sconfitta".